https://doi.org/10.5194/egusphere-2026-2856
Preprint. Discussion started: 5 June 2026

Analysis of systematic biases in equatorial resolved and parameterized wave forcing of the quasi-biennial oscillation in a multi-model ensemble

Hyun-Kyu Lee[1], James A. Anstey[2], Hye-Yeong Chun[1], Shingo Watanabe[3,4], Francois Lott[5], Zhaoyang Chai[6,7], Yixiong Lu[6], Qi Tang[8], Jinbo Xie[8,9], Dong-Chan Hong[10], Seok-Woo Son[10], Federico Serva[11], Pu Lin[12,13], Martin B. Andrews[14], Neal Butchart[14], Aleena M. Jaison[15,16], Jeff R. Knight[14], Scott Osprey[17], Hiroaki Naoe[18], Kohei Yoshida[18], Yoshio Kawatani[19], and Jadwiga H. Richter[20]

[1]Department of Atmospheric Sciences, Yonsei University, Seoul, South Korea
[2]Canadian Centre for Climate Modelling and Analysis (CCCma), Victoria, Canada
[3]Japan Agency for Marine-Earth Science and Technology (JAMSTEC), Yokohama, Japan
[4]Advanced Institute for Marine Ecosystem Change (WPI-AIMEC), Tohoku University, Sendai, Japan
[5]Laboratoire de Météorologie Dynamique (LMD), Paris, France
[6]Earth System Modeling and Prediction Centre, China Meteorological Administration (CMA), Beijing, China
[7]Institute of Atmospheric Physics, Chinese Academy of Sciences (CAS), Beijing, China
[8]Lawrence Livermore National Laboratory, Livermore, CA, United States
[9]High Meadows Environmental Institute (HMEI), Princeton University, Princeton, NJ, USA
[10]School of Earth and Environmental Sciences, Seoul National University, Seoul, Korea
[11]Institute of Marine Sciences, National Research Council (CNR-ISMAR), Italy
[12]Geophysical Fluid Dynamics Laboratory (NOAA), Princeton, NJ, USA
[13]Department of Earth and Environmental Sciences, Boston College, MA, USA
[14]Met Office Hadley Centre (MOHC), Exeter, UK
[15]Atmospheric, Oceanic and Planetary Physics, University of Oxford, Oxford, United Kingdom
[16]Department of Physics, Imperial College London, United Kingdom
[17]National Centre for Atmospheric Science (NCAS), University of Oxford, Oxford, UK
[18]Meteorological Research Institute (MRI), Tsukuba, Japan
[19]Faculty of Environmental Earth Science, Hokkaido University, Sapporo, Japan
[20]National Center for Atmospheric Research (NCAR), Boulder, USA

Correspondence to: Hyun-Kyu Lee (leehk20@yonsei.ac.kr), James A. Anstey (james.anstey@ec.gc.ca)

Abstract. The equatorial resolved and parameterized wave forcing of the quasi-biennial oscillation (QBO) in models participating in phase 2 of the Atmospheric Processes and their Role in Climate (APARC) Quasi-Biennial Oscillation initiative (QBOi) is analyzed. We compare two experiments performed by the multi-model ensemble, NoNudge and ObsQBO, covering the period from 1979 to 2020. In this study, NoNudge designates experiments where the QBO is generated internally without nudging, whereas ObsQBO represents experiments in which the QBO is bias-corrected by nudging stratospheric zonal-mean zonal winds toward ERA5, allowing investigation of modelling uncertainties originating from biases in the background winds. While the NoNudge simulations exhibit QBO biases typically seen in models,

https://doi.org/10.5194/egusphere-2026-2856
Preprint. Discussion started: 5 June 2026

including eastward wind bias in the mid-stratosphere and underestimation of the QBO amplitude in the lower stratosphere, these discrepancies are effectively mitigated by nudging in ObsQBO simulations. In the NoNudge experiments, the models reveal weaker Kelvin and gravity wave forcing in the tropical lower stratosphere than ERA5, but these forcings are enhanced in the ObsQBO experiment, suggesting that weak wave forcing of internally generated QBOs results from reduced critical-level filtering of waves due to unrealistically weak vertical wind shear at these levels. However, in ObsQBO experiments, the models still exhibit insufficient Kelvin and gravity wave forcing in the lower stratosphere. This suggests that the weak QBO amplitude in the lower stratosphere may stem from the inherent deficit in wave forcing in the models. One notable feature of the ObsQBO experiments is the excessive eastward wave forcing in the mid-to-upper stratosphere during the easterly QBO phase in the lower tropical stratosphere. The correlation coefficient between the 10 hPa eastward wave forcing and westerly QBO amplitude is 0.8, indicating that excessive westerly QBO is associated with strong eastward wave forcing in the mid-to-upper stratosphere.

1 Introduction

In the equatorial stratosphere, there is a phenomenon of alternating downward propagations of easterly and westerly winds, known as the quasi-biennial oscillation (QBO), which accounts for most of the variability observed in the equatorial stratosphere (Baldwin et al., 2001). The QBO influences various equatorial phenomena, such as the Madden-Julian oscillation (MJO) (Jin et al., 2023; Yoo and Son, 2016), tropical convection (Andrews et al., 2024; Lee et al., 2019; Liess and Geller, 2012; Rodrigo et al., 2025), and the semi-annual oscillation (SAO) (Smith et al., 2022; 2023). Moreover, the influence of the QBO extends beyond the tropics, modifying the Brewer–Dobson circulation (BDC) (Veenus and Das, 2025) and influencing the polar vortex via the Holton–Tan effect (Anstey et al., 2022; Garfinkel et al., 2012; Holton and Tan, 1980).

Because the QBO exerts global-scale influences (via teleconnections), accurate prediction of the QBO is recognized as an important factor for improving subseasonal weather predictions (Garfinkel et al., 2018). Moreover, because the QBO is expected to change in response to the warming climate (Lee et al., 2024; Richter et al., 2022), accurate simulation of the QBO is crucial for producing reliable future-climate projections of its impacts. However, it is well known that generating a realistic QBO in atmospheric models remains highly challenging. In the Coupled Model Intercomparison Project phase 6 (CMIP6), only approximately half of the general circulation models (GCMs) were able to simulate the QBO, and its spatial characteristics were not significantly improved compared to CMIP5 (Richter et al., 2020). In phase 1 of the Atmospheric Processes And their Role in Climate (APARC) QBO initiative (QBOi), which provided the first comprehensive multi-model intercomparison of QBO resolving GCMs, including an analysis of QBO wave driving (Holt et al., 2022)[1]. It was found that

[1] QBOi phase-1 studies are collected in a QBO Modelling Intercomparison Special Issue available at https://rmets.onlinelibrary.wiley.com/doi/toc/10.1002/(ISSN)1477-870X.qbo-modelling-intercomparison.

https://doi.org/10.5194/egusphere-2026-2856
Preprint. Discussion started: 5 June 2026

GCMs in the QBOi multi-model ensemble exhibited common biases when compared with the observed QBO, such as weak easterly phase amplitude near 50 hPa (Bushell et al., 2022). While these systematic biases are now well known, their specific causes are not well understood.

The downward propagation of the QBO is mainly driven by momentum deposition from equatorial waves (Holton and Lindzen, 1972; Lindzen and Holton, 1968; Match and Fueglistaler, 2021; Plumb and Bell, 1982) and tropical upwelling, which is part of the BDC, partially offsets the wave-driven QBO descent (Pahlavan et al., 2021a). The descent of the easterly QBO (EQBO) is mainly driven by gravity waves (GWs), whereas the descent of the westerly QBO (WQBO) is largely driven by both Kelvin waves and GWs (Kang et al., 2018; Kim and Chun, 2015b; Pahlavan et al., 2021b). Additionally, extratropical Rossby waves and GWs contribute to driving the BDC including its tropical upwelling (Kang et al., 2020b). Therefore, a realistic representation of wave propagation and dissipation in the global middle atmosphere is required to accurately simulate the QBO.

Despite the importance of accurately representing wave dynamics, it is unclear which components of wave forcing in GCMs are unrealistic and how they could be improved. One reason for this is the difficulty in identifying the origins of uncertainties in wave forcing. The wave forcing in the equatorial stratosphere is influenced by both the wave source and background wind. Holt et al. (2022) compared the wave forcing in 13 models and found that strong convectively coupled Kelvin waves (CCKWs) do not guarantee strong resolved eastward mean-flow forcing in the equatorial stratosphere. Because the background winds differ among the models, it is difficult to identify the reasons underlying these findings. Furthermore, the drag of the non-orographic GW (NOGW), which is essential for driving the QBO in most GCMs, diverges in the QBOi models; however, the underlying cause remains unexplored (Bushell et al., 2022). Consequently, it is unclear whether the uncertainties in resolved and unresolved wave forcing originate mainly from the wave sources, the background winds, the mechanisms of wave dissipation in the stratosphere, or all of these.

One possible approach to address one of these factors is to nudge the model-led equatorial stratospheric zonal wind toward the observed wind to isolate uncertainties originating from the background wind (García-Franco et al., 2023). The phase-2 of QBOi provides a multi-model framework to evaluate how systematic QBO biases influence wave dynamics and simulated climate responses (Anstey et al., 2026). In QBOi phase-2, nudging experiments were conducted in which the zonal wind in the equatorial stratosphere was nudged toward ECMWF Reanalysis v5 (ERA5; Hersbach et al., 2020). The purpose of the present study is to address two key questions. First, to quantify the extent to which realistic background zonal wind can improve modelled equatorial wave forcing. Second, to quantify the residual biases in wave forcing that remain under the accurate background wind condition. The remainder of this paper is structured as follows. Section 2 describes the data and methodology. The results are presented in Section 3, and the discussion is presented in Section 4. Finally, Section 5 presents a summary and conclusion.

https://doi.org/10.5194/egusphere-2026-2856
Preprint. Discussion started: 5 June 2026

2 Data and methodology

2.1 Models

In this study, Exp1 and Exp1-ObsQBO experiments of QBOi phase-2 are used. Exp1 is essentially the Atmospheric Model Intercomparison Project (AMIP) experiment, which was conducted over 42 years from 1979 to 2020. The 41-year dataset from 1980 to 2020 is used in GFDL-ESM4. The sea surface temperature (SST) and sea ice from CMIP6 are prescribed. Because Exp1 does not include zonal wind nudging, the QBOs exhibited by the QBOi models in this experiment are generated internally. In the Exp1-ObsQBO experiment, the zonal-mean zonal winds in the models are nudged toward the zonal-mean zonal winds of ERA5 in the equatorial stratosphere. Equatorial waves in the troposphere are not constrained by the nudging. However, because full-field nudging is applied to three models (E3SMv2 (Golaz et al. (2022), EC-Earth3, and GFDL-ESM4), equatorial waves with periods longer than the relaxation timescale (5 days) may be constrained to follow ERA5 when they propagate into the tropical stratosphere. In this study, 11 QBOi models are used, and each model provided 1–3 ensemble members. Detailed information is provided in Table 1. Some details of model resolution and physics, and references to model documentation papers, are provided by Anstey et al. (2026). Exp1 and Exp1-ObsQBO are denoted as NoNudge and ObsQBO hereinafter, respectively.

Table 1: Summary of the QBOi phase-2 models used in this study. The numbers indicate the number of ensemble members for each individual QBOi model. F denotes that the model used full-field nudging. H denotes that the model provided high-frequency data (6-hourly). GRIMs4.0 did not submit the Exp1 experiments because it does not internally generate the QBO. EC-Earth3 high-frequency data are available following a 1.5° regular latitude-longitude remapping.

Model	Institution	Ensemble size	
		ObsQBO	NoNudge
[H]BCC-CSM2-MR	China Meteorological Administration	3	3
CAS-ESM	Institute of Atmospheric Physics Chinese Academy of Sciences	3	3
[HF]E3SMv2	Lawrence Livermore National Laboratory	3	3
[HF]EC-Earth3	EC-Earth Consortium	1	1
[F]GFDL-ESM4	Geophysical Fluid Dynamics Laboratory	3	3
[H]GRIMs4.0	Seoul National University	1	-
HadGEM3GA7-1	Met Office Hadley Centre	3	3
[H]LMDz6	Laboratoire de Météorologie Dynamique	3	1
[H]MIROC6.1, p1	Japan Agency for Marine-Earth Science and Technology	3	3
[H]MIROC6.1, p2	Japan Agency for Marine-Earth Science and Technology	3	3
MRI-ESM2.0	Meteorological Research Institute	3	3

https://doi.org/10.5194/egusphere-2026-2856
Preprint. Discussion started: 5 June 2026

2.2 Reanalyses and observation data

We use ERA5 data as a reference dataset. Because waves with short vertical wavelengths are filtered out when using relatively coarse vertical resolution pressure-level data (Kim and Chun, 2015b), the model-level data are used in this study. The horizontal resolution of ERA5 is 0.25° with 137 vertical levels, and the time interval is 3 h. We performed the analysis using the native resolution of ERA5. Modern-Era Retrospective analysis for Research and Applications, Version 2 (MERRA2; Gelaro et al., 2017) data are additionally used for the analysis of wave forcing, given that inconsistencies in the momentum budget exist between reanalyses (Fujiwara et al., 2022; Serva et al., 2024). MERRA2 model-level data have a horizontal resolution of 0.625° × 0.5° (longitude × latitude) with 72 vertical levels and a 3-hourly time interval. The Global Precipitation Climatology Project (GPCP) Version 3.3 daily precipitation data are used as the reference dataset for the power spectra of precipitation (Huffman et al., 2025). The horizontal resolution of the GPCP data is 0.5°.

2.3 Identification of the QBO phase

We use two different methods to define the QBO phases. The first approach is that the WQBO and EQBO phases are classified using a QBO index (Kang et al., 2018; Lee et al., 2019; Naoe et al., 2025). The time series of the normalized zonal wind is obtained by subtracting the climatology from the monthly averaged zonal wind at 30 hPa averaged between 5°N and 5°S and dividing it by the standard deviation. The months when the normalized zonal wind is greater than 0.5 are classified as WQBO, whereas those when the normalized zonal wind is less than −0.5 are classified as EQBO. Second, the descending westerly (DW) and descending easterly (DE) are defined as the onset of the westerly and easterly of the monthly averaged zonal wind at 30 hPa averaged between 5°N and 5°S, respectively (Garcia and Richter, 2019; Lee et al., 2024). Smoothing is not applied to define the QBO phases, unlike when calculating the QBO metrics. To avoid short-duration oscillations of the wind about zero, cases in which the magnitude of the zonal wind does not exceed 2 m s^{-1} at each QBO phase are neglected.

2.4 QBO analysis methods

To examine the QBO characteristics in the QBOi phase-2 models, the QBO amplitude, period, and latitudinal and vertical extent are calculated, similar to the evaluation of the QBOi phase-1 models described by Bushell et al. (2022). To define the QBO metrics, the time series of the five-month smoothed zonal wind averaged between 5°N and 5°S is used. In cases where the three ensembles exist, the QBO metrics are obtained by calculating the metrics from the individual ensembles and subsequently performing the ensemble mean. The calculation procedures for the individual QBO indices are described below.

https://doi.org/10.5194/egusphere-2026-2856
Preprint. Discussion started: 5 June 2026

2.4.1 QBO period

We calculate the QBO period using two methods: the fast Fourier transform (FFT) and QBO transition times (TT) methods. For the FFT method, the period at each level is defined as the period at which the spectral peak of the time series of the zonal wind occurs. Subsequently, the QBO period is obtained by averaging the periods obtained for all levels from 50 to 10 hPa. For the TT method, the times at which the zonal wind transitions from easterly to westerly winds at 10 hPa are recorded, and the period for each QBO cycle is then estimated based on the intervals between these transition times. Detailed explanations of the FFT and TT methods are provided in previous studies (Bushell et al., 2022; Lee et al., 2024; Richter et al., 2022).

2.4.2 QBO amplitude

We calculate the QBO amplitude using two methods. First, the vertical structure of the QBO amplitude is obtained based on Stockdale et al. (2022). From 1979 to 2020, the 10 most westerly and most easterly zonal-mean zonal winds at each level are selected. These are then averaged to obtain the vertical profile of the amplitude of westward and eastward winds. Second, the amplitude is measured based on the TT method, as described in Bushell et al. (2022). The eastward QBO amplitude is defined as the maximum zonal wind at each level (10 and 50 hPa) reached between the onset of a westerly at 10 hPa and its subsequent transition to an easterly at 10 hPa. Conversely, the westward QBO amplitude is defined as the magnitude of the minimum zonal wind reached between the onset of an easterly and its subsequent transition to a westerly. The QBO amplitude for each cycle is then defined as the mean of its westward and eastward QBO amplitudes. The mean QBO amplitude is obtained by calculating the amplitude for each QBO cycle and averaging them across all cycles.

2.4.3 QBO vertical and latitudinal extent

The vertical and latitudinal extent of the QBO is determined using the Bushell et al. (2022) method and is briefly summarized as follows. The vertical extent of the QBO is determined using the QBO amplitude calculated by using the TT method for each individual QBO cycle. The upper level is chosen as either the altitude at which the maximum QBO amplitude occurs or 10 hPa, whichever is lower. A half level is identified at the altitude where the QBO amplitude is half of the amplitude at the upper level. The distance between the upper and half levels is then defined as the vertical extent of the QBO. The latitudinal extent is obtained from the full width at half maximum (FWHM) of the QBO amplitude within 20°, derived from a Gaussian fit. In this study, the latitudinal extent is calculated using the time series of zonal wind anomalies with the seasonal cycle removed. This is because the QBO amplitude at 50 hPa for NoNudge experiments is much smaller than the seasonal cycle of the zonal wind in several models. When the Gaussian fit is applied to the raw winds without removing the seasonal cycle, a physically reasonable QBO width cannot be obtained.

https://doi.org/10.5194/egusphere-2026-2856
Preprint. Discussion started: 5 June 2026

2.5 Transformed Eulerian mean momentum equation

The detailed analysis of wave forcing in the models is conducted based on the transformed Eulerian mean (TEM) equation (Andrews et al., 1987) in log-pressure coordinates:

$$\frac{\partial \bar{u}}{\partial t} = \hat{f}\bar{v}^* - \bar{w}^* \frac{\partial \bar{u}}{\partial z} + \frac{1}{\rho_0 a cos\phi} \nabla \cdot F + \bar{X}_{OGW} + \bar{X}_{NOGW} + F_{Nudging} + Res, \quad (1)$$

where $\hat{f}$ represents the modified Coriolis parameter, $\hat{f} = f - (acos\phi)^{-1}(\bar{u}cos\phi)_\phi$; $\bar{v}^*$ indicates the residual meridional velocity, defined as $\bar{v}^* = \bar{v} - \rho_0^{-1}(\rho_0 \overline{v'\theta'}/\bar{\theta}_z)_z$; ρ_0 is the air density; a is the radius of the Earth; $\bar{w}^*$ represents the residual vertical velocity, defined as $\bar{w}^* = \bar{w} + (acos\phi)^{-1}(cos\phi \overline{v'\theta'}/\bar{\theta}_z)_\phi$; and F and $\nabla \cdot F$ represent the Eliassen–Palm flux (EPF) and divergence of the EPF (EPFD), respectively, and F is defined as $F = (0, F^\phi, F^z)$. The meridional and vertical components of EPF are $F^\phi = \rho_0 a cos\phi(\bar{u}_z \frac{\overline{v'\theta'}}{\bar{\theta}_z} - \overline{u'v'})$ and $F^z = \rho_0 a cos\phi(\hat{f} \frac{\overline{v'\theta'}}{\bar{\theta}_z} - \overline{u'w'})$, respectively. $\bar{X}_{OGW}$ and $\bar{X}_{NOGW}$ represent parameterized orographic and non-orographic GW drag, respectively, $F_{Nudging}$ indicates the tendency due to nudging, and Res is the residual term of the zonal momentum in Eq. (1).

To simplify the analysis of Eq. (1), it is rewritten as follows:

$$\frac{\partial \bar{u}}{\partial t} = ADV + EPFD + \bar{X}_{param} + \bar{X}_{imbalance}, \quad (2)$$

where ADV is the zonal wind tendency caused by advection, defined as $ADV = \hat{f}\bar{v}^* - \bar{w}^* \frac{\partial \bar{u}}{\partial z}$; $EPFD$ is the tendency due to divergence of the EPF, which represents resolved wave forcing; $\bar{X}_{param}$ is the sum of $\bar{X}_{OGW}$ and $\bar{X}_{NOGW}$; and $\bar{X}_{imbalance}$ is obtained by subtracting ADV, $EPFD$, and $\bar{X}_{param}$ from the zonal wind tendency.

2.6 Equatorial wave separation method

Equatorial wave separation is performed to quantify the individual resolved wave forcing in the QBOi models. The methodology used here is revised based on Kim and Chun (2015a), with the addition of a classification for small-scale gravity (SSG) waves. The detailed procedure is as follows. Initially, a 90-day window function is applied to all anomalies of variables used to calculate the EPF (i.e., u', v', w', and θ'). The structure of the window function involves a sine component for the first 30 days, unity throughout the middle 30 days, and a cosine component for the final 30 days. We then conduct a two-dimensional Fourier transform on these variables to obtain the zonal (k) and frequency (ω) spectra at each latitude. After separating the symmetric and antisymmetric components, the calculation of the EPF is performed on each spectrum (Kim and Chun, 2015a). To maintain the original variance, the EPF is multiplied by a factor of 1.5. EPFD is obtained using the EPF for each wavenumber and frequency spectra. After the EPFD calculation is complete, if the wavenumber exceeds 20, it is classified as SSG waves (Ern et al., 2021; Kim, 2025; Pahlavan et al., 2021b), whereas if it is below 21, it is classified as planetary waves (PWs).

https://doi.org/10.5194/egusphere-2026-2856
Preprint. Discussion started: 5 June 2026

PWs are categorized into Kelvin, mixed Rossby–gravity (MRG), Rossby, and inertia-gravity (IG) waves. For the symmetric spectra, if $|F^{z1}| < |F^{z2}|$, where F^{z1} and F^{z2} represent the first and second terms of $F^z = \rho_0 a cos\phi \left(\hat{f} \frac{\overline{v'\theta'}}{\overline{\theta}_z} - \overline{u'w'} \right) = F^{z1} + F^{z2}$, respectively, spectral components with $\omega < 0.75$ cycle day^{-1} and $k > 0$ are classified as Kelvin waves. For the antisymmetric spectra, if $F^{z1} \times F^{z2} < 0$, spectral components with $0.1 \leq \omega \leq 0.5$ cycle day^{-1} are classified as MRG waves. From the remaining components that are not classified as Kelvin and MRG waves, those with $\omega \leq 0.4$ cycle day^{-1} are classified as Rossby waves. Finally, all remaining components, except for the diurnal and semidiurnal tides, are classified as IG waves. Wave forcings of diurnal and semidiurnal tides are negligible in the QBO regime (not shown).

https://doi.org/10.5194/egusphere-2026-2856
Preprint. Discussion started: 5 June 2026

3 Results

3.1 QBO characteristics in the QBOi models

The QBO characteristics in the QBOi models are compared with those of ERA5. Figure 1 shows the vertical structure of the westward and eastward QBO amplitudes. In the NoNudge experiments, none of the models reproduce the westward winds of ERA5 between 10 and 50 hPa (Fig. 1a). At 10 hPa, the multi-model mean (MMM) of −33.0 m s^{-1} is much smaller in magnitude than that of ERA5 (−42.2 m s^{-1}). For the eastward QBO amplitude, the MMM is larger than that of ERA5 above 20 hPa. At 10 hPa, the MMM is 21.2 m s^{-1}, substantially higher than the ERA5 value of 16.8 m s^{-1}. However, this difference is largely influenced by models with extreme amplitudes, such as CAS-ESM and GFDL-ESM4. Excluding these two models reduces the MMM to 18.0 m s^{-1}, indicating that the discrepancy is smaller than that found for the westward QBO amplitude. Between 20 and 30 hPa, the MMM is comparable to ERA5, reflecting the offset between two models (CAS-ESM and GFDL-ESM4) with large amplitudes and the majority of models with smaller amplitudes. Below 30 hPa, the eastward QBO amplitude is smaller than that of ERA5, except for three models (CAS-ESM, GFDL-ESM4, and MRI-ESM2.0). Table 2 presents the QBO amplitude calculated using the TT method. Because the GCMs exhibit both weak westward and eastward amplitudes in the lower stratosphere (Fig. 1a), they produce weak QBO amplitudes (Table 2). At 50 hPa, only MRI-ESM2.0 lies within 1 standard deviation (SD) σ of ERA5 (for eastward, westward, and QBO amplitude), whereas the remaining models produce weaker QBO amplitudes.

In the ObsQBO experiments, most of the wind biases seen in the NoNudge experiments are mitigated, and the vertical structure of the zonal winds in MMM and in most individual models closely resembles that of ERA5 (Fig. 1b). Specifically, the insufficient magnitude of the westward wind is substantially improved, with the MMM at 10 hPa increasing from −33.0 to −39.1 m s^{-1}. The TT amplitude also shows notable improvements, with more than half of the models distributed within 1σ of the ERA5 amplitude at both 10 and 50 hPa (Table 2). This result is expected given that full-strength nudging is applied between 10 and 70 hPa (Anstey et al., 2026). However, the magnitude of the westward wind in BCC-CSM2-MR is too weak, whereas the eastward wind in CAS-ESM is too strong (Fig. 1b). Although the 5-day nudging time scale is employed, some models show incomplete relaxation toward ERA5 winds, and the exact causes remain unclear. The eastward QBO amplitude above 10 hPa does not differ substantially from that in the NoNudge experiments (Fig. 1b). This behavior is consistent with the experimental design, in which the nudging coefficient is progressively reduced above 10 hPa, becoming zero at 5 hPa.

https://doi.org/10.5194/egusphere-2026-2856
Preprint. Discussion started: 5 June 2026

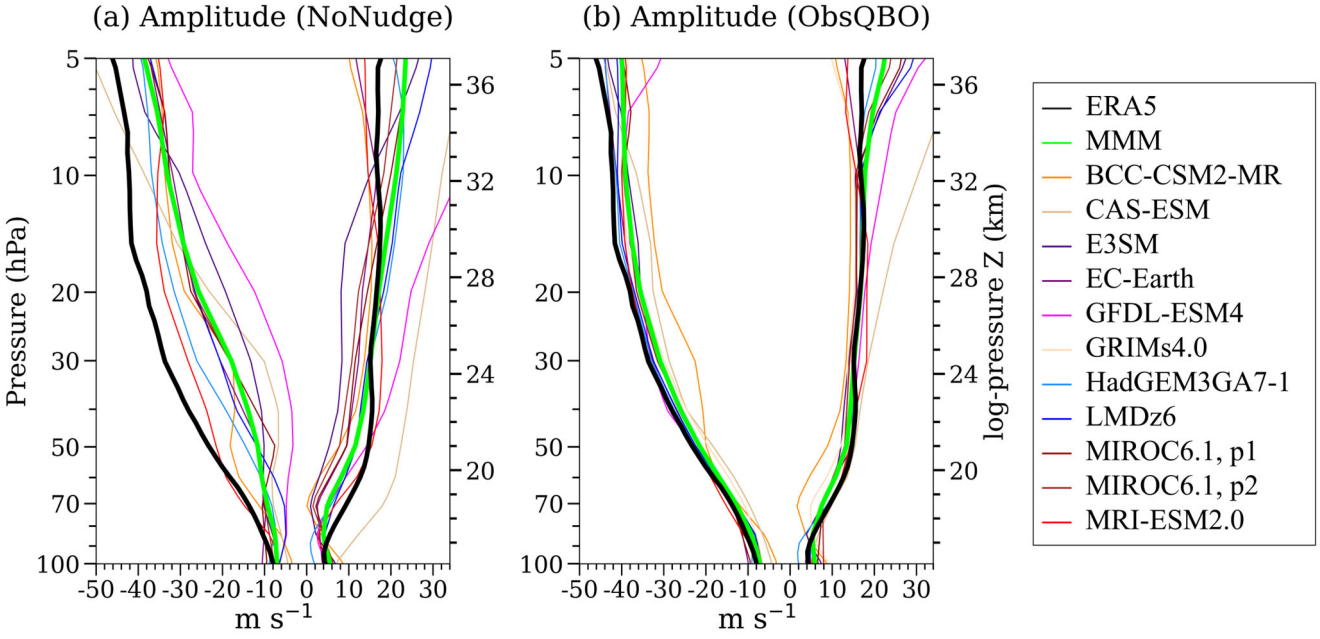

Figure 1: Vertical structures of the QBO amplitude in (a) NoNudge and (b) ObsQBO experiments. The zonal winds averaged between 5°S and 5°N from 1979 to 2020 are used to calculate the QBO amplitude based on the Stockdale et al. (2022) method. The QBO amplitude is obtained by averaging the 10 maxima and minima zonal winds at each level, which is then plotted as a vertical profile for the models (thin coloured lines) and ERA5 (thick black lines).

Table 2: Metrics of the QBO amplitude. Bold text indicates that the value is within 1 standard deviation of ERA5. Values in parentheses denote the amplitudes of the WQBO and EQBO phases, respectively. The ERA5 amplitudes are shown together with their ±1 standard deviation.

	TT amplitude at 10 hPa (m s^{-1})		TT amplitude at 50 hPa (m s^{-1})	
Model	NoNudge (W / E)	ObsQBO (W / E)	NoNudge (W / E)	ObsQBO (W / E)
BCC-CSM2-MR	18.2 (8.1 / 28.3)	18.7 (8.7 / 28.8)	8.4 (2.4 / 14.5)	10.7 (4.7 / **16.7**)
CAS-ESM	**24.9** (26.8 / 22.9)	20.8 (23.3 / 18.4)	10.5 (18.3 / 2.7)	12.5 (**11.6** / 13.4)
E3SMv2	12.7 (5.3 / 20.0)	20.1 (9.1 / 31.0)	4.8 (2.1 / 7.6)	12.8 (9.2 / **16.4**)
EC-Earth3	16.2 (8.9 / 23.5)	**22.6** (**11.3** / **33.9**)	7.2 (6.9 / 7.4)	**14.2** (**11.2** / **17.3**)
GFDL-ESM4	18.0 (24.2 / 11.9)	**23.0** (14.9 / 31.1)	6.8 (**11.0** / 2.6)	**13.7** (**11.1** / **16.2**)
GRIMs4.0	No	**21.8** (10.0 / **33.5**)	No	11.9 (8.6 / 15.1)
HadGEM3GA7-1	**25.4** (18.3 / **32.5**)	**22.8** (**11.1** / **34.5**)	9.4 (8.7 / 10.2)	**14.3** (**11.2** / **17.4**)
LMDz6	**22.7** (18.7 / 26.7)	**22.6** (**11.4** / **33.7**)	6.5 (5.5 / 7.5)	**14.1** (**11.2** / **17.1**)
MIROC6.1, p1	20.8 (16.3 / 25.3)	**21.6** (**11.0** / **32.2**)	5.2 (6.8 / 3.6)	**13.5** (**10.2** / **16.9**)
MIROC6.1, p2	**21.1** (14.0 / 28.2)	**21.7** (**10.8** / **32.7**)	6.5 (5.1 / 7.8)	**13.5** (**10.1** / **16.9**)
MRI-ESM2.0	20.0 (8.6 / **31.5**)	20.6 (8.3 / **32.9**)	**14.8** (**12.2** / **17.5**)	**14.4** (**10.4** / **18.3**)
Multi-model mean	20.0 (14.9 / 25.1)	**21.5** (**11.8** / **31.1**)	8.0 (7.9 / 8.1)	**13.2** (**10.0** / **16.5**)
ERA5	23.2±2.2 (11.9±1.8 / 34.6±3.5)		14.6±1.5 (11.3±1.5 / 17.9±2.1)	

https://doi.org/10.5194/egusphere-2026-2856
Preprint. Discussion started: 5 June 2026

Metrics of the vertical and latitudinal extent of the QBO are shown in Table S1. The vertical depth of the QBO varies among the models in the NoNudge experiments, ranging from 5.1 to 9.1 km. Five models have shallower QBOs than ERA5, and five are close to ERA5 (within 1σ). The latitudinal widths of QBOi models are mostly smaller than those of ERA5 at 10 and 50 hPa. The metrics of all models agree almost universally with ERA5 in the ObsQBO experiments; notably the latitudinal extent at 50 hPa falls within 1σ of ERA5 across all models.

Table 3: Metrics of the QBO period. Bold text indicates that the value is within 1 standard deviation of ERA5. Values in parentheses denote the durations of the WQBO and EQBO phases, respectively. The QBO periods of ERA5 are shown together with their ±1 standard deviation.

(month)	FFT period (50–10 hPa average)		TT period (reference level: 10 hPa)	
Model	NoNudge	ObsQBO	NoNudge (W / E)	ObsQBO (W / E)
BCC-CSM2-MR	20.4	25.4	22.9 (5.4 / **17.5**)	**27.5** (6.6 / **20.9**)
CAS-ESM	29.6	28.0	**30.1** (18.1 / 12.0)	**27.4** (**8.6** / **18.7**)
E3SMv2	22.5	28.0	39.7 (**7.9** / 31.8)	**29.0** (**9.0** / **20.1**)
EC-Earth3	22.9	28.0	22.4 (**8.1** / **14.3**)	**29.1** (**9.7** / **19.4**)
GFDL-ESM4	29.2	28.3	18.9 (**12.1** / 6.8)	**27.4** (**11.3** / **16.2**)
GRIMs4.0	No	28.0	No	**29.1** (**9.3** / **19.8**)
HadGEM3GA7-1	30.3	28.0	**30.4** (**10.8** / **19.5**)	**29.1** (**9.8** / **19.3**)
LMDz6	28.0	28.0	**27.8** (14.3 / 13.5)	**29.1** (**10.0** / **19.1**)
MIROC6.1, p1	26.7	28.0	**30.0** (17.4 / 12.6)	**29.1** (**10.1** / **19.0**)
MIROC6.1, p2	26.4	28.0	**27.0** (12.4 / **14.6**)	**29.1** (**9.9** / **19.2**)
MRI-ESM2.0	26.5	28.0	**26.5** (7.2 / **19.3**)	**29.1** (7.3 / **21.8**)
Multi-model mean	26.3	27.8	**27.6** (**11.4** / **16.2**)	**28.6** (**9.2** / **19.4**)
ERA5	28.0		29.1±4.8 (10.0±2.4 / 19.1±4.8)	

Table 3 presents the QBO period calculated using the FFT and TT methods applied to ERA5 and the QBOi models. The QBO period of ERA5 reveals a longer duration for the easterly phase at 10 hPa, with a WQBO period of 10 months and the EQBO period of 19.1 months. It is well recognized that the EQBO persists longer in the upper regime of the QBO (Baldwin et al., 2001; Kim, 2025). Table 3 shows that HadGEM3GA7-1 is the only model that realistically simulates both the period and phase asymmetry of the QBO in the NoNudge experiment (as defined by the period of both QBO phases and the total period being within one standard deviation of ERA5). The QBO periods calculated using the TT and FFT methods are similar for all models except E3SMv2 and GFDL-ESM4. To determine the QBO period using the TT method, the onset of both westerly and easterly phases must be clearly resolved in the simulation, as in the observed QBO. If very weak winds alternate between easterlies and westerlies in the model simulation, the TT method produces a biased estimate, thereby diagnosing a shorter QBO period. In this study, cases where the wind between QBO cycles was less than 2 m s^{-1} are excluded to prevent the QBO period from being inaccurately measured due to excessively weak winds. However, in E3SMv2, the QBO amplitude occasionally fails to exceed 2 m s^{-1} (Fig. S1). Such weak amplitude limits the identification of

https://doi.org/10.5194/egusphere-2026-2856
Preprint. Discussion started: 5 June 2026

distinct QBO cycles. Consequently, the application of the TT method to E3SMv2 leads to a longer QBO period than that obtained using the FFT method (Table 3). For GFDL-ESM4, the EQBO amplitude is 11.9 m s^{-1}, less than half of ERA5 (Table 2). The descent of the SAO frequently generates cases where the onset of the westerly exceeds the EQBO winds (Fig. S1), which consequently shortens the QBO period calculated using the TT method (Table 3). Measurements calculated using the FFT method is more robust against these model biases, allowing for a more consistent representation of the QBO period in QBOi models (but without being able to distinguish separately the durations of the WQBO and EQBO phases). For ObsQBO experiments, all models except BCC-CSM2-MR exhibit QBO periods of 28 months for the FFT method. The periods for the TT method fall within 1σ of ERA5 for all models.

A summary of the QBO characteristics is represented by grading the models with respect to how closely they agree with ERA5 (Fig. 2 and Fig. S2). Following Bushell et al. (2022), the grade g is calculated as:

$$g = 1 - \frac{|m - m_{ref}|}{3\sigma_{ref}}. \quad (3)$$

Here m and m_{ref} are the model mean and the ERA5 mean, respectively, and σ_{ref} is the standard deviation of ERA5. When the model and ERA5 means are in perfect agreement, $g = 1$. Conversely, if the difference between the two exceeds $3\sigma_{ref}$, g is set to 0. Therefore, g values closer to 1 indicate better model performance.

The evaluation metrics include the same diagnostics evaluated in QBOi phase-1: the QBO period, amplitude at 10 and 50 hPa, latitudinal extent at 10 and 50 hPa, and depth. Most of the metrics in ObsQBO experiments are similar to those of ERA5 (Fig. 2). For the QBO amplitude at 10 and 50 hPa, more than half of the models achieve a grade exceeding 0.67. However, BCC-CSM2-MR, CAS-ESM, and E3SM still do not produce realistic QBO amplitudes (Table 2). Nevertheless, considering that the grade of amplitude at 50 hPa is lower than 0.1 for all models except MRI-ESM2.0 in the NoNudge experiments (Fig. S2), the ObsQBO results show much closer agreement with ERA5, as expected (Fig. 2). The mean grade is improved in ObsQBO compared with NoNudge for all models, with the MMM increasing from 0.46 to 0.87. Consequently, with the zonal winds constrained by nudging to closely follow ERA5 in ObsQBO, biases in the background wind are strongly reduced.

https://doi.org/10.5194/egusphere-2026-2856
Preprint. Discussion started: 5 June 2026

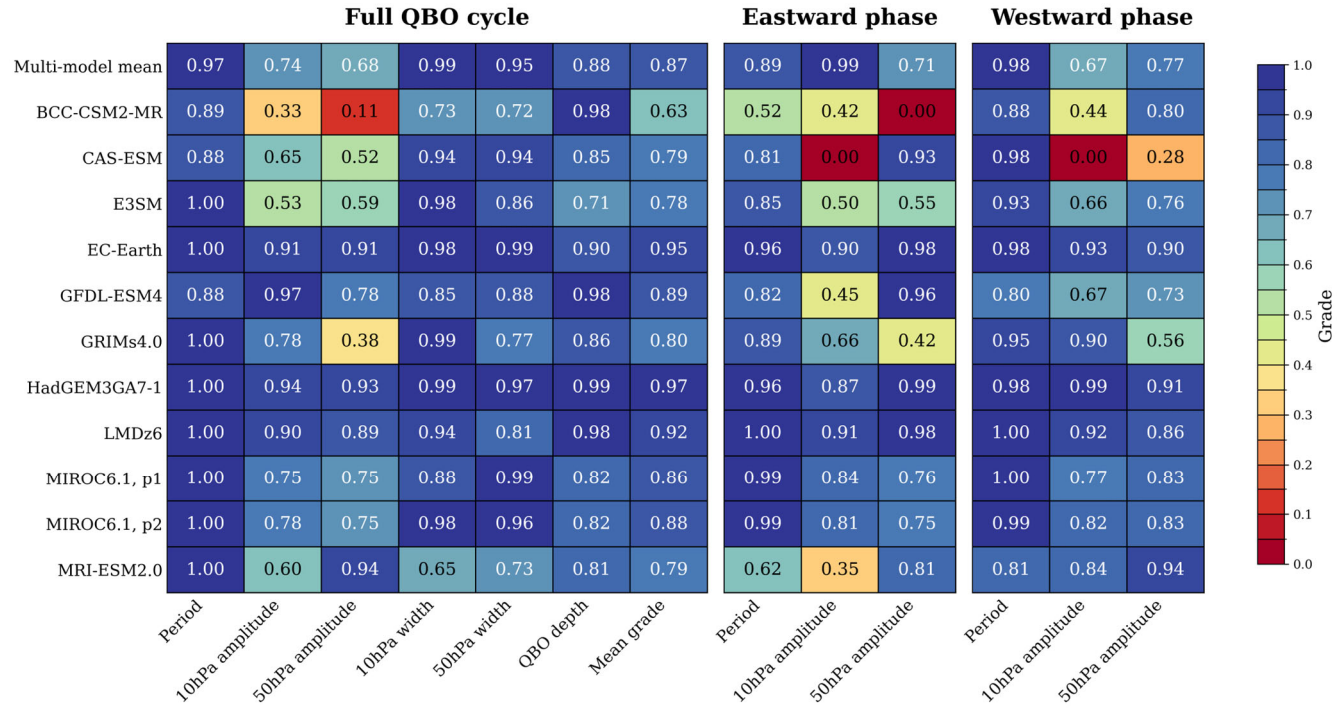

Figure 2: Quantitative grades comparing the QBOi models against ERA5 for the ObsQBO experiments. A value of 1 indicates that the model and ERA5 agree perfectly. A value of 0 indicates that the model bias exceeds three times the standard deviation of ERA5. White text indicates that these values are within one standard deviation of ERA5. Detailed calculation processes are described in Section 3.1 and following Bushell et al. (2022). Corresponding results for the NoNudge experiments are shown in Fig. S2.

https://doi.org/10.5194/egusphere-2026-2856
Preprint. Discussion started: 5 June 2026

3.2 Tropical precipitation and wind power spectra

Next, the power spectra of the QBOi models are compared with those of the observations. The power spectra of precipitation rate and zonal wind are calculated by applying a 90-day window to the daily mean data, centered on the middle day of each individual month (Kang et al., 2020a). GPCP precipitation data for 23 years from 1998 to 2020 and ERA5 zonal wind data for 42 years from 1979 to 2020 are used as reference datasets.

3.2.1 Power spectral density of precipitation

Figures 3 and 4 present the power spectral density (PSD) of the precipitation for symmetric and antisymmetric components, respectively. For the symmetric spectra, GPCP and ERA5 exhibit dominant signals within the eastward-propagating wave region, specifically between the equivalent depths of 8 and 40 m (Fig. 3). The CCKW signals are observed in the equatorial troposphere (Chien and Kim, 2023; Lee et al., 2025; Wheeler and Kiladis, 1999), and they may serve as a source of the eastward momentum required to drive the QBO. The ERA5 signal closely resembles GPCP, although its power spectra is comparatively smaller. In the NoNudge experiments, the eastward propagating wave signals in the models exhibit a large distribution, as observed in previous studies (Holt et al., 2022; Lott et al., 2014). BCC-CSM2-MR presents excessively strong power, whereas several models (CAS-ESM, EC-Earth3, LMDz6, and MIROC6.1-p2) present weaker power. Two models (HadGEM3GA7-1 and MIROC6.1-p1) exhibit a coherent signal comparable to that observed. Although the magnitude varies, the ratio of the raw power spectra to the background spectra, calculated following Wheeler and Kiladis (1999), shows a peak around an equivalent depth of 40 m, confirming that wave organization is well-captured in the models. For the antisymmetric spectra, a pronounced peak associated with the MRG waves appears in GPCP near the equivalent depth of 40 m, and a similar feature is also observed in ERA5 (Fig. 4). The observed MRG signal is not well represented in most models, except for HadGEM3GA7-1 and MIROC6.1-p1.

The differences between the ObsQBO and NoNudge experiments are very small in both the symmetric and antisymmetric spectra. Several factors could contribute to this minimal impact on the spectra, despite the nudging of observed QBO winds. First, there is a possibility that the representation of downward influence of QBO is weak in climate models. García-Franco et al. (2023) showed that even when nudging the QBO winds, insufficient stratosphere-troposphere coupling could hinder surface impacts. Second, the power spectra in this study are averaged over a 23-year period, which may suppress the QBO signals. However, when the power spectra are separated by individual QBO phases, the differences remain negligible (not shown). Consequently, nudging applied in the equatorial stratosphere has a limited impact on the tropospheric source, allowing the stratospheric wave forcing to be examined with minimal influence from changes in tropospheric sources.

https://doi.org/10.5194/egusphere-2026-2856
Preprint. Discussion started: 5 June 2026

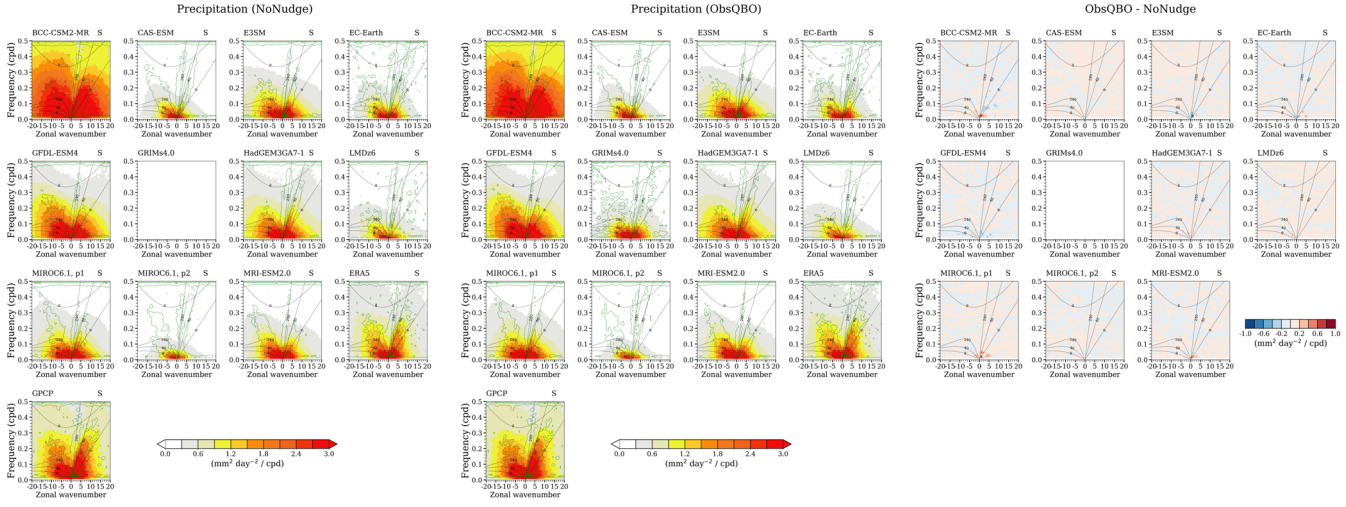

Figure 3: Power spectral density (PSD) results for symmetric components of the precipitation rate in (left) NoNudge, (center) ObsQBO experiments, and (right) their differences, shown as a function of zonal wavenumber and frequency averaged between 10°N and 10°S. The PSD for precipitation rate is averaged between 1998 and 2020. The PSDs of ERA5 and GPCP are plotted as references. The black dashed lines present the dispersion relations of each equatorial wave for the equivalent depths of h = 8, 40, and 240 m. "cpd" indicates the cycles per day. The green contours indicate values where the ratio of the raw power spectrum to the background spectrum, calculated following Wheeler and Kiladis (1999), exceeds 1, with a contour interval of 0.2.

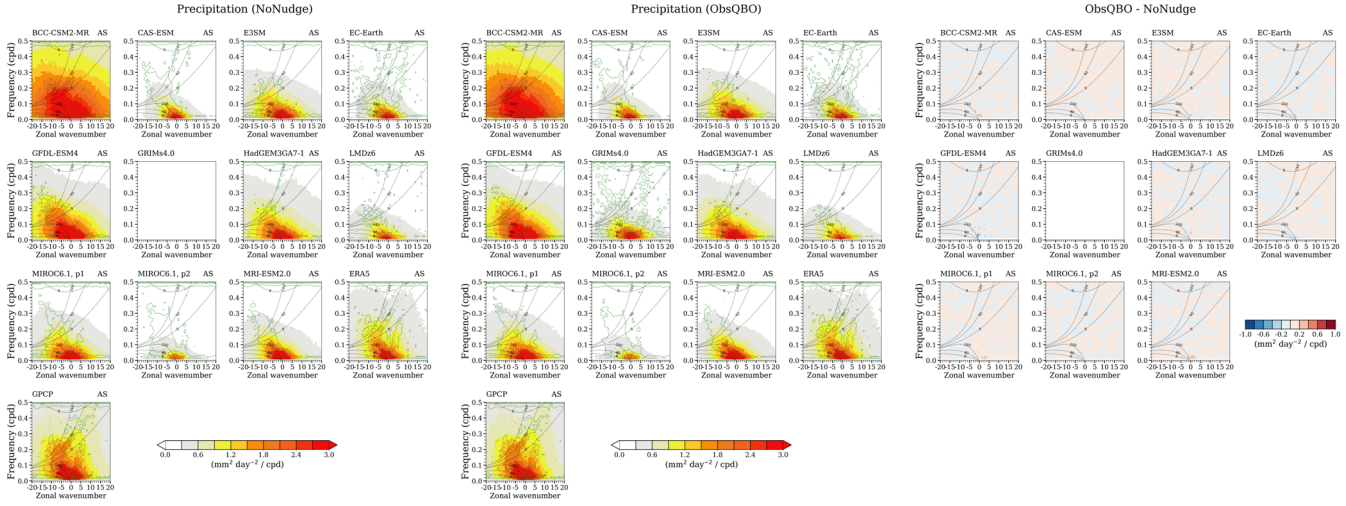

Figure 4: Same as Fig. 3 but for antisymmetric components.

https://doi.org/10.5194/egusphere-2026-2856
Preprint. Discussion started: 5 June 2026

3.2.2 Power spectral density of the zonal wind

Figure 5 shows the PSD for the symmetric components of the daily-mean zonal wind at 50 hPa. In the NoNudge experiments, the power spectra of the models have magnitudes comparable to those of ERA5, and the spectral peaks of all models are located between the equivalent depths of 40 and 240 m. These results differ from the finding that the PSDs of precipitation widely vary, which is attributable to the fact that the wave signal in the equatorial stratosphere is influenced not only by the wave source but also by the background winds (Holt et al., 2022). A notable feature in the nudging experiments is the suppression of the eastward-propagating wave signal in the ObsQBO compared to NoNudge, except for CAS-ESM. As the PSDs of zonal wind at 100 hPa exhibit negligible differences (not shown), the increased westerly wind in the lower stratosphere in ObsQBO may filter eastward-propagating waves more strongly than in NoNudge. Notably, in the three models where full-field nudging is applied (E3SMv2, EC-Earth3, and GFDL-ESM4), overall wave signals are weakened in ObsQBO more strongly than in the other models (Fig. 5), suggesting a possible damping effect on wave development by full-field nudging, and noting that much of the weakening occurs for frequencies less than 0.2 cpd (recalling that the nudging timescale is 5 days).

The power spectra of the zonal wind for antisymmetric components are shown in Fig. 6. The MRG wave signals in the NoNudge experiments are well represented in the models, exhibiting a spectral peak at an equivalent depth of 40 m. Notably, several models (CAS-ESM, LMDz6, and MIROC6.1-p1) exhibit a stronger MRG wave signal than that in ERA5, although their precipitation spectra are smaller than those of ERA5 (Fig. 4). While the wave filtering by the background wind may contribute to this phenomenon, another potential source is the in-situ generation of planetary waves near the QBO jet (Garcia and Richter, 2019; Kang et al., 2020a; Lee et al., 2024; Mahó et al., 2025). Unlike the symmetric spectrum, nudging produces inconsistent effects on MRG waves across the models, leading to either suppression or amplification. One possible reason for this is the modulation of barotropic instability as the QBO amplitude and latitudinal extent are nudged toward more realistic QBO structures. Garcia and Richter (2019) proposed that MRG waves are generated to neutralize the instability of the westerly QBO jet.

To explore the potential relationship between MRG waves and the modulation of barotropic instability by nudging, the frequency of the meridional gradient of the potential vorticity $\bar{q}_\phi$ in the equatorial stratosphere is investigated for individual QBO phases. $\bar{q}_\phi$ is calculated as follows (Andrews et al., 1987):

$$\bar{q}_\phi = 2\Omega cos\phi - \left[\frac{(\bar{u}cos\phi)_\phi}{acos\phi}\right]_\phi - \frac{a}{\rho_0}\left(\frac{\rho_0 f^2}{N^2}\bar{u}_z\right)_z, \quad (4)$$

where Ω and N present the rotation of the Earth and Brunt–Väisälä frequency, respectively. Table 4 shows the modulation of instability in five models (BCC-CSM2-MR, E3SMv2, LMDz6, MIROC6.1-p1, and MIROC6.1-p2), which provided high-frequency data (Table 1). Although EC-Earth3 also provided high-frequency data, it was excluded from the wave analysis because the combination of a coarse remapped resolution and full-field nudging limits the diagnosis of equatorial wave biases. During the WQBO phase, the probability of negative $\bar{q}_\phi$ occurrences is reduced in four models (BCC-CSM2-MR,

https://doi.org/10.5194/egusphere-2026-2856
Preprint. Discussion started: 5 June 2026

LMDz6, MIROC6.1-p1, and MIROC6.1-p2) when nudging is applied, whereas it increases in E3SMv2. The change in $\bar{q}_\phi$ is predominantly governed by the change in the meridional curvature of the zonal wind (the second term in Eq. 4; not shown). Concurrent with these responses, the MRG wave signal decreases in the four models, with the most evident decreases observed in LMDz6 and MIROC6.1-p1, whereas it increases in E3SMv2 (Fig. S3). This relationship is unclear during the EQBO phase (Table 4; Fig. S4). A possible explanation for the increased frequency of $\bar{q}_\phi$ in E3SMv2 is the improvement of its underestimated WQBO amplitude through nudging (Table 2). Consequently, a realistic WQBO structure could be an important factor to accurately reproduce the MRG waves in the equatorial stratosphere.

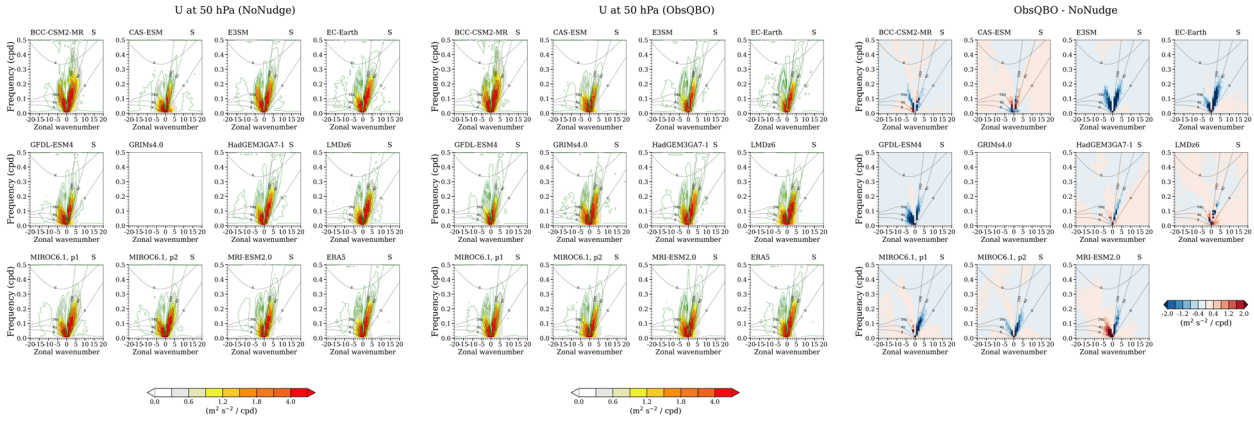

Figure 5: Power spectral density (PSD) results for the symmetric components of the zonal wind at 50 hPa for (left) NoNudge, (middle) ObsQBO experiments, and (right) their differences, shown as a function of zonal wavenumber and frequency averaged between 10°N and 10°S. The PSD for zonal wind is averaged between 1979 and 2020. The PSD of ERA5 is plotted as a reference. The black dashed lines present the dispersion relations of each equatorial wave for the equivalent depths of h = 8, 40, and 240 m. "cpd" refers to the cycles per day. The green contours indicate values where the ratio of the raw power spectrum to the background spectrum, calculated following Wheeler and Kiladis (1999), exceeds 1, with a contour interval of 0.2.

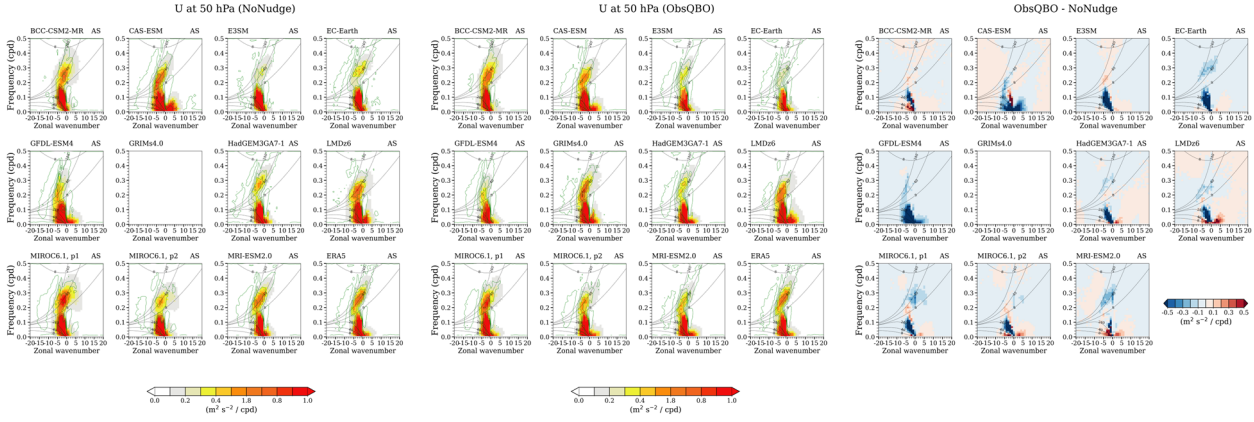

Figure 6: Same as Fig. 5 but for antisymmetric components.

https://doi.org/10.5194/egusphere-2026-2856
Preprint. Discussion started: 5 June 2026

Table 4: Frequency of negative $\bar{q}_\phi$ occurrence in the lower QBO regime (13°S–13°N, 30–70 hPa). Bold values indicate cases where the probability of negative $\bar{q}_\phi$ occurrence decreases in ObsQBO compared to NoNudge experiments. All values are shown as percentages.

		BCC-CSM2-MR	E3SMv2	LMDz6	MIROC6.1, p1	MIROC6.1, p2
WQBO	NoNudge	3.3	0.2	6.3	3.8	3.8
	ObsQBO	**2.5**	0.5	**3.7**	**1.5**	**2.2**
EQBO	NoNudge	0.7	0.1	3.8	5.1	3.4
	ObsQBO	0.7	0.3	4.6	**1.2**	**2.1**

3.3 TEM momentum budget in the equatorial region

The momentum budget of the QBOi models is examined through the individual TEM components (Eq. 2). Figure 7 shows the differences between the WQBO and EQBO composites of the TEM components. The TEM components during the individual phases of WQBO and EQBO are shown in Figs. 8 and 9, respectively. The WQBO-EQBO difference in zonal wind of MMM at 30 hPa is 20.8 m s^{-1} in NoNudge, which is significantly smaller than 35.0 m s^{-1} in ERA5 (Fig. 7a), but the WQBO-EQBO difference at 30 hPa increases to 32.7 m s^{-1} in ObsQBO (Fig. 7f). The improvement in the vertical structure of the EQBO via nudging accounts for this change (Figs. 8k and 9k). The most pronounced difference between NoNudge and ObsQBO in the zonal wind tendency occurs below 30 hPa (Fig. 7l). At 50 hPa, the models' zonal wind tendency ranges from 0.04 to 0.11 m s^{-1} day^{-1} (except for 0.18 m s^{-1} day^{-1} in MRI-ESM2.0), which is much smaller than 0.17 m s^{-1} day^{-1} in ERA5 (Fig. 7b). This reflects the poor downward propagation of the QBO in many of these models (Fig. S1) and their weak QBO amplitudes in the lower stratosphere (Table 2).

The advection (ADV) (Fig. 7c) has a sign opposite to that of the zonal wind tendency (Fig. 7b), which corresponds to the slowdown of the downward propagation of the QBO induced by tropical upwelling. The ADV is predominantly controlled by vertical advection in the QBO regime (Figs. S5 and S6). In the lower stratosphere, the magnitudes of ADV in models are much smaller in NoNudge experiments. This discrepancy is attributed to the smaller vertical wind shear during the EQBO phase (Fig. S6). Nudging the zonal wind eliminates this bias (Fig. 9), aligning the ADV structure with ERA5 (Fig. 7h).

In contrast to the ADV, the wave forcing terms have the same sign as the zonal wind tendency, confirming their role as the primary driver of the QBO (Figs. 7b, 7d, and 7e). All QBOi models show substantially weaker EPFD than ERA5 (Fig. 7d), with a particular difference in westward forcing (Figs. 8 and 9). In ObsQBO, the amplitude of the EPFD remains smaller than that of ERA5 (Fig. 7i) although it does increase slightly compared to NoNudge (Fig. 7n). Notably, the magnitude of EPFD in MERRA2 is comparable to that in the QBOi models (Figs. 7d and 7i). In this study, the resolution in the zonal direction of MERRA2 is 0.625°, which is coarser than that of ERA5. The horizontal resolution of ERA5 is

https://doi.org/10.5194/egusphere-2026-2856
Preprint. Discussion started: 5 June 2026

approximately 30 km (Hersbach et al., 2020), which is finer than that of any model used in this study, and this fine resolution allows ERA5 to explicitly resolve more SSG waves. SSG waves that are not fully resolved by GCMs can be represented through the appropriate use of NOGW parameterization. In the NoNudge experiments, the vertical structure of $\bar{X}_{param}$ is similar to the EPFD of ERA5 (Fig. 7e). Furthermore, the zonal wind tendency in GCMs is primarily driven by $\bar{X}_{param}$, confirming that the QBO simulation depends strongly on the GW parameterization (Figs. 7b and 7e).

Nevertheless, the wave forcing is insufficient in the lower stratosphere to produce a realistic QBO, even with the inclusion of $\bar{X}_{param}$ (Fig. 7a). Therefore, the improvement of the QBO in ObsQBO is driven by the nudging forcing. When nudging is applied, the MMM of $\bar{X}_{param}$ at 50 hPa increases from 0.07 to 0.13 m s^{-1} day^{-1}, which could be explained by enhanced vertical wind shear in the lower stratosphere that facilitates more critical-level filtering of vertically propagating waves (Fig. 7j). Second, $\bar{X}_{param}$ at 10 hPa in NoNudge exhibits a large distribution, ranging from −0.08 to −0.54 m s^{-1} day^{-1} (Fig. 7e), which aligns with the findings of the QBOi phase-1 models (Bushell et al., 2022). Unlike in the lower stratosphere, nudging leads to an increase in $\bar{X}_{param}$ in the upper stratosphere during the EQBO phase (Fig. 9o). This is likely due to the more realistic easterly wind during the EQBO phase, allowing for more eastward-propagating waves to propagate upward and break (Fig. 9). The implications of this for the QBO amplitude are further discussed in Sect. 4.1.

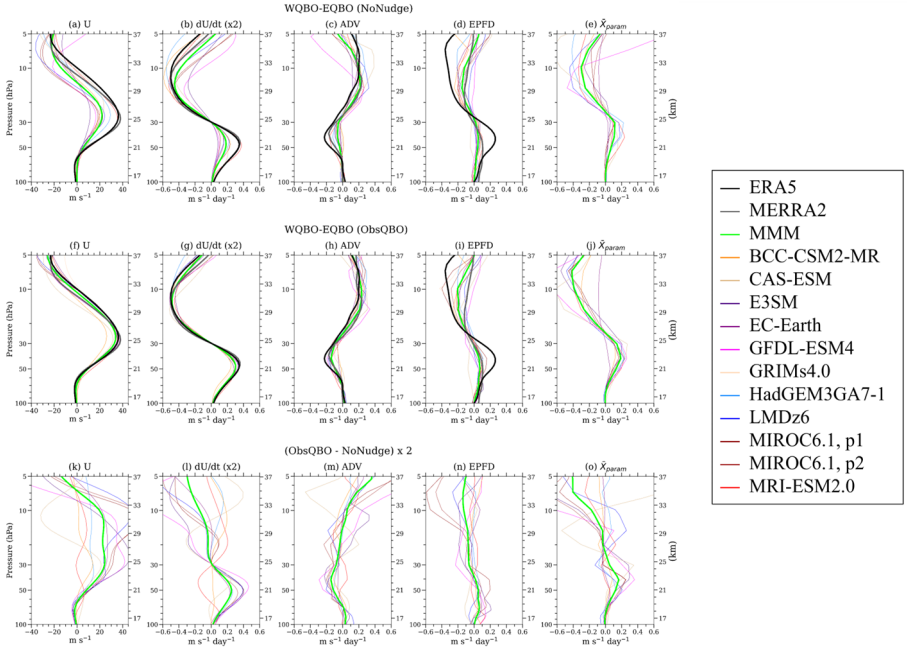

Figure 7: Differences between the westerly QBO (WQBO) and easterly QBO (EQBO) composites of the TEM components averaged between 5°S and 5°N for (top) NoNudge, (middle) ObsQBO, and (bottom) their differences. From left to right, the panels show the (a, f, k) zonal wind, (b, g, l) zonal wind tendency, (c, h, m) time tendency of the zonal wind caused by advection, (d, i, n) resolved wave forcing, and (e, j, o) parameterized GW forcing. For clarity, the TEM components in ObsQBO minus NoNudge are multiplied by two.

https://doi.org/10.5194/egusphere-2026-2856
Preprint. Discussion started: 5 June 2026

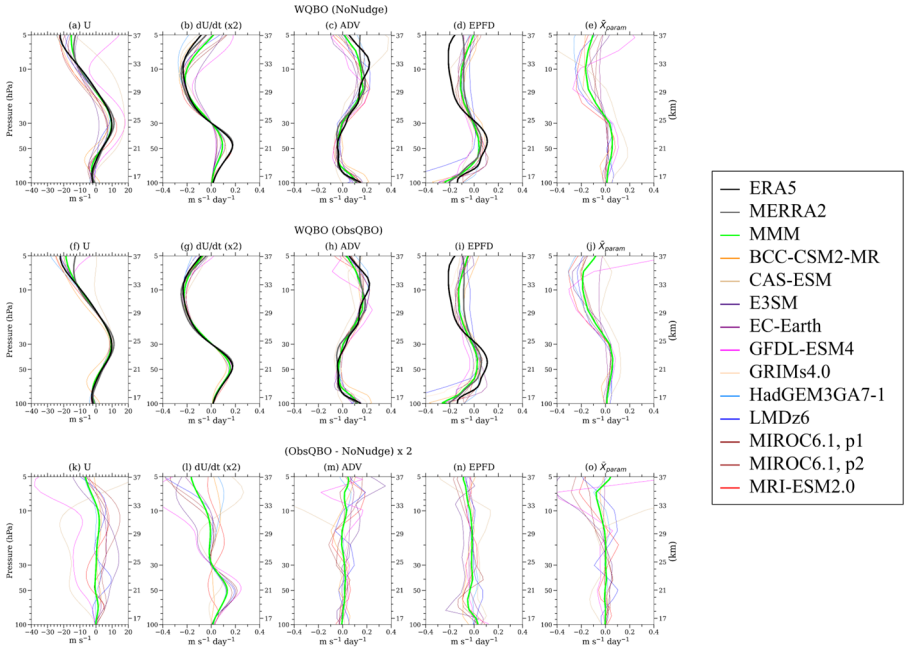

Figure 8: Composites of the TEM components averaged between 5°S and 5°N during the WQBO phases for (top) NoNudge, (middle) ObsQBO, and (bottom) their differences. From left to right, the panels show the (a, f, k) zonal wind, (b, g, l) zonal wind tendency, (c, h, m) time tendency of the zonal wind caused by advection, (d, i, n) resolved wave forcing, and (e, j, o) parameterized GW forcing. For clarity, the TEM components in ObsQBO minus NoNudge are multiplied by two.

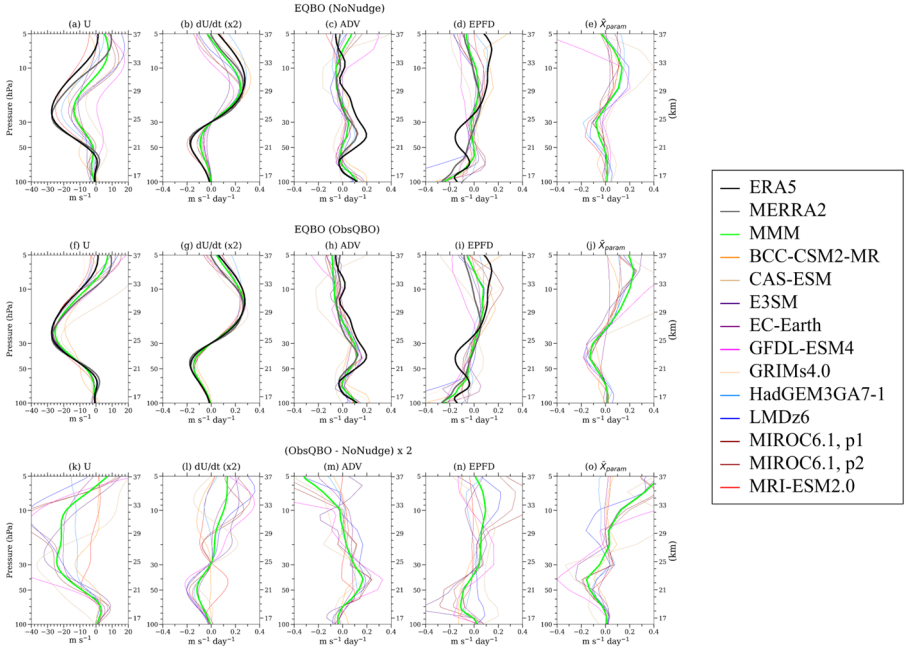

Figure 9: Same as Fig. 8 but for the EQBO phases.

https://doi.org/10.5194/egusphere-2026-2856
Preprint. Discussion started: 5 June 2026

3.4 Equatorial wave forcing

The momentum budget analysis indicates that the discrepancies of GCMs relative to reanalysis mainly arise from differences in wave forcing. Because wave forcing arises from multiple wave types, we use the equatorial wave separation method based on Kim and Chun (2015a), as described in Sect. 2.6, to examine the contribution of each wave component. We use five models (BCC-CSM2-MR, E3SMv2, LMDz6, MIROC6.1-p1, and MIROC6.1-p2) to analyze the equatorial wave forcing. To focus on the analysis of wave forcing, the TEM equation is reformulated from Eq. (2) as follows:

$$\frac{\partial \bar{u}}{\partial t} = ADV + \bar{X}_{PW} + SSG + \bar{X}_{param} + \bar{X}_{imbalance} = ADV + \bar{X}_{PW} + \bar{X}_{GW.model} + \bar{X}_{imbalance}, \quad (6)$$

$$\bar{X}_{PW} = EPFD(k < 21), \quad (7)$$

$$SSG = EPFD(k > 20), \quad (8)$$

$$\bar{X}_{GW.model} = SSG + \bar{X}_{param}, \quad (9)$$

where $\bar{X}_{PW}$ and SSG represent the planetary wave forcing and the resolved small-scale GW forcing, respectively. $\bar{X}_{GW.model}$ denotes the total GW forcing, calculated as the sum of the resolved and parameterized GW forcings.

While the magnitude of EPFD in ERA5 is larger than that in QBOi models (Figs. 8 and 9), its magnitude is insufficient to drive the QBO (Kim, 2025). To address this limitation, the reference GW drag, $\bar{X}_{GW.ref}$, for validating $\bar{X}_{GW.model}$ is defined as follows:

$$\bar{X}_{GW.ref} = \frac{\partial \bar{u}}{\partial t} - ADV - \bar{X}_{PW}, \quad (10)$$

$$\bar{X}^{*}_{GW.ref} = \left(\frac{\partial \bar{u}}{\partial t} - ADV\right)_{MERRA2} - \bar{X}_{PW}, \quad (11)$$

where $\bar{X}_{GW.ref}$ is calculated for each reanalysis (ERA5 and MERRA2) by subtracting the sum of the zonal wind tendency caused by advection and the planetary wave forcing from the total zonal wind tendency (Ern et al., 2021). Because the variability of the residual vertical velocity in ERA5 is known to be excessive compared to observations (Ming et al., 2025), an additional reference GW drag $\bar{X}^{*}_{GW.ref}$, which is calculated using $\frac{\partial \bar{u}}{\partial t}$ and ADV from MERRA2 and $\bar{X}_{PW}$ from ERA5 following an approach similar to that of Kim and Chun (2015b), is also presented.

3.4.1 Equatorial planetary wave forcing

Figures 10 and 11 show the equatorial wave forcing during the WQBO and EQBO phases, respectively. Below 50 hPa, Kelvin waves provide eastward forcing, whereas Rossby and MRG waves provide westward forcing regardless of the QBO phase (Figs. 10 and 11). The westward and eastward forcings largely offset each other, and the residual westward forcing acts in the upper troposphere and lower stratosphere (UTLS) (Figs. 8 and 9). Between 10 and 50 hPa, the magnitude of the westward forcing by MRG and Rossby waves is smaller than that of GWs (Fig. 11). The relatively weak magnitude of westward forcing by planetary waves implies that momentum deposition by GWs is the primary driver for the downward propagation of the EQBO, in agreement with previous studies (Kang et al., 2018; Kim and Chun, 2015b; Pahlavan et al.,

https://doi.org/10.5194/egusphere-2026-2856
Preprint. Discussion started: 5 June 2026

2021b). While MRG waves do not serve as the primary driver of the QBO, they play an important role in QBO dynamics by alleviating instability near the QBO jet (Garcia and Richter, 2019) and by providing prerequisite conditions for the QBO disruption event (Kang et al., 2020a). IG waves provide westward forcing in the westward wind shear zone during WQBO, albeit with small magnitudes (Figs. 10d and 10k). In other cases, the magnitude of IG wave forcing is negligible.

The vertical structure of Kelvin wave forcing at altitudes above 70 hPa depends on the QBO phase. During the WQBO phase, Kelvin waves provide eastward forcing below 20 hPa, with a magnitude comparable to that of GW forcing (Figs. 10a and 10e). This indicates that Kelvin waves serve as one of the primary drivers for the downward descent of the WQBO. In the WQBO phase, the Kelvin wave forcing in GCMs aligns well with reanalyses, and the impact of nudging on its vertical structure is not strong (Fig. 10o). During the EQBO phase, Kelvin wave forcing is close to zero between 30 and 50 hPa (Figs. 11a and 11h), which is associated with a westward wind shear region that is unfavorable for the breaking of eastward-propagating waves (Fig. S6). Above 30 hPa, it provides eastward forcing, contributing to the onset and descent of the WQBO in the upper EQBO region where wind shear is eastward (Fig. 9a). In the NoNudge experiments, the Kelvin wave forcing is broadly overestimated between 10 and 50 hPa compared to the reanalyses during the EQBO phase (Fig. 11a). By contrast, the eastward forcing bias in ObsQBO experiments is more vertically localized, with forcing intensifying sharply near 10 hPa (Fig. 11h). At this level, the MMM of Kelvin wave forcing is 0.15 m s^{-1} day^{-1}, which is approximately 60% larger than that in ERA5. This discrepancy suggests that the improved representation of easterly winds through nudging likely allows more eastward-propagating waves to reach the upper QBO region and dissipate. The strong eastward forcing in the models arises because their Kelvin wave momentum flux exhibits more substantial dissipation than that of ERA5 in the upper stratosphere, regardless of the magnitude of the momentum flux in the lower stratosphere (Fig. S7). One possible explanation is related to the limited vertical resolution of the models. Most GCMs used in this study have relatively coarse vertical resolution in the upper stratosphere, exceeding 1 km (Fig. 2 in Anstey et al., 2026). Such resolution is insufficient to adequately resolve Kelvin waves with short vertical wavelengths (Richter et al., 2014). The dispersion relation of tropical Kelvin waves is as follows (Ern et al., 2009):

$$\hat{c}_{px} = \frac{\hat{\omega}}{k} = -\frac{N}{m} = -N\frac{\lambda_z}{2\pi} \tag{12}$$

where $\hat{\omega}$ is intrinsic frequency; k and m are the horizontal and vertical wavenumbers, respectively; λ_z is vertical wavelength; $\hat{c}_{px}$ is intrinsic horizontal phase speed. For $N = 0.02$ s^{-1} and $\lambda_z = 4$ km (~$4\Delta z$), $\hat{c}_{px}$ is approximately 13 m s^{-1}. Therefore, Kelvin waves with intrinsic phase speeds smaller than this speed are more affected by artificial dissipation. Nevertheless, clarifying the detailed mechanisms is beyond the scope of this study and requires further investigation.

https://doi.org/10.5194/egusphere-2026-2856
Preprint. Discussion started: 5 June 2026

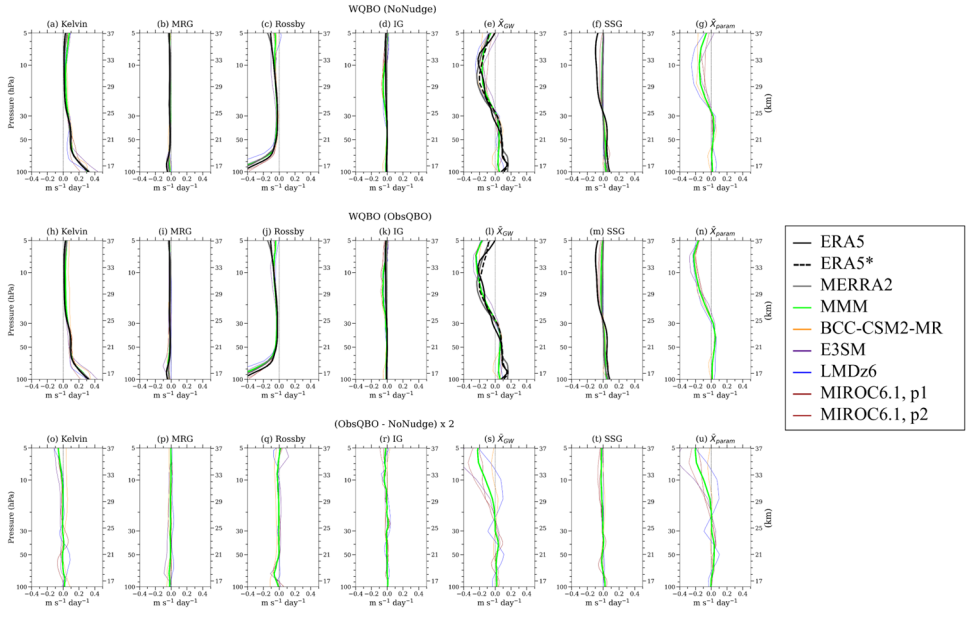

Figure 10: Composites of wave forcings averaged between 5°S and 5°N during the WQBO phases for (top) NoNudge, (middle) ObsQBO, and (bottom) their differences. From the left, wave forcings of (a, h, o) Kelvin waves, (b, i, p) MRG waves, (c, j, q) Rossby waves, (d, k, r) IG waves, (e, l, s) GWs, (f, m, t) small-scale GWs, and (g, n, u) parameterized GWs. Wave forcings of ObsQBO minus NoNudge are multiplied by two to facilitate comparison. The thick black dashed lines, labeled as ERA5*, indicate $\bar{X}^{*}_{GW.ref}$ of ERA5 (using MERRA2 $\frac{\partial \bar{u}}{\partial t}$ and ADV; see text for details). The thin black dashed line in each panel indicates a zero baseline.

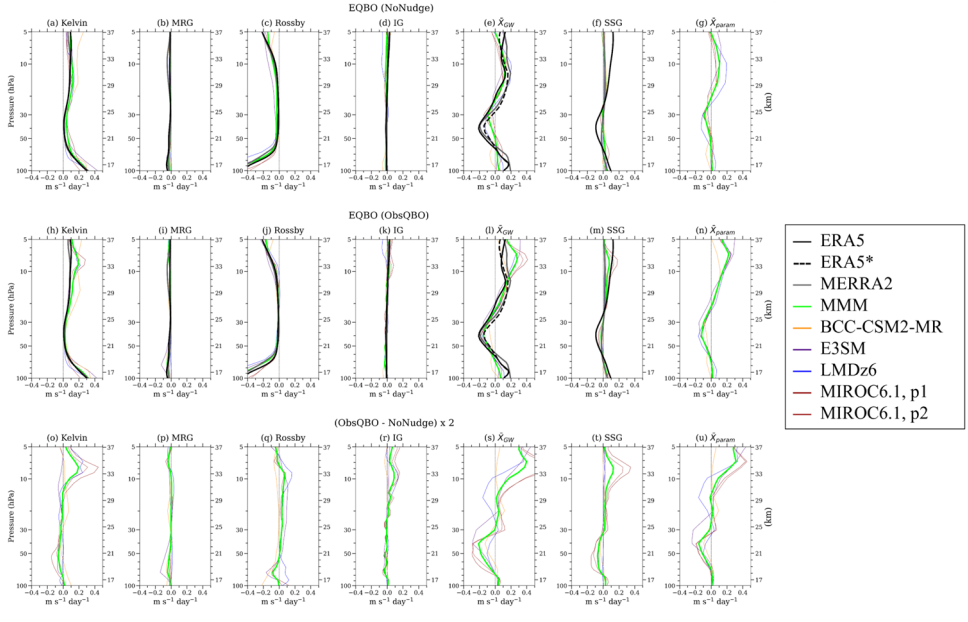

Figure 11: Same as Fig. 10 but for the EQBO phases.

https://doi.org/10.5194/egusphere-2026-2856
Preprint. Discussion started: 5 June 2026

While composite analysis based on WQBO and EQBO allows the examination of the wave forcing at QBO boundaries, it has limitations in revealing the forcing when the QBO descends. The phase separation into descending westerly and easterly components, as introduced in Sect. 2.3, provides an effective framework for examining wave forcing at the specific moment of QBO descent. Figures 12 and 13 show the equatorial wave forcing during the DW and DE phases, respectively. Except for the Kelvin wave, the magnitude of the wave forcing by other planetary waves is not substantial between 10 and 50 hPa. During the DW phase, the Kelvin wave forcing in ERA5 reached a local maximum of 0.30 m s^{-1} day^{-1} between 30 and 40 hPa, whereas the MMM in the NoNudge experiments showed a significantly lower value of 0.13 m s^{-1} day^{-1} (Fig. 12a). In the ObsQBO experiments, the Kelvin wave forcing in the lower stratosphere is enhanced (Fig. 12o); however, the magnitude in most models remains lower than in the reanalyses (Fig. 12h). Nevertheless, LMDz6 and MIROC6.1-p1 show magnitudes of 0.27 and 0.29 m s^{-1} day^{-1}, respectively, which are comparable to that in ERA5. During the DE phase, the planetary wave forcing within the QBO region, including Kelvin waves, is very weak in both NoNudge and ObsQBO experiments, although MRG make a small contribution at 30–50 hPa (Fig. 13).

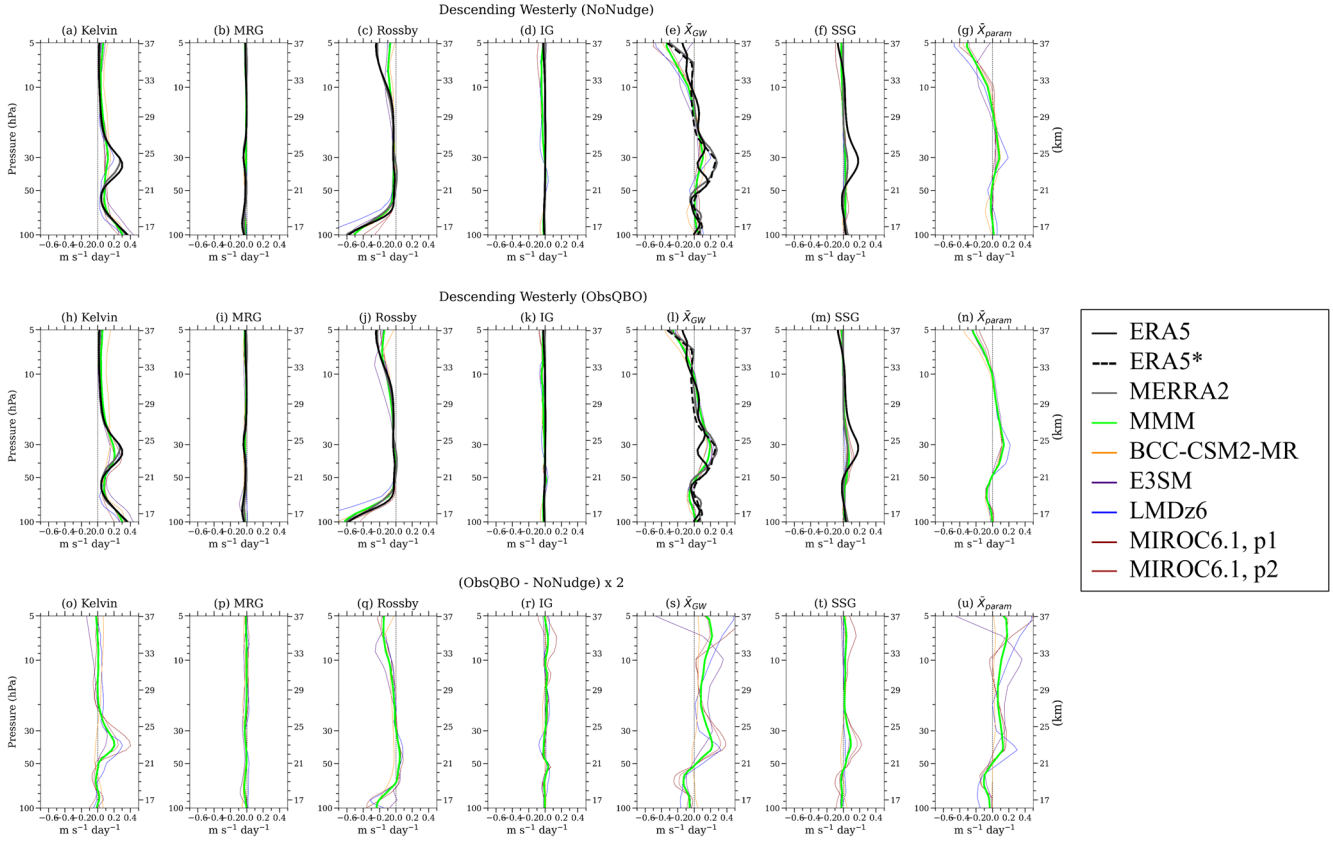

Figure 12: Same as Fig. 10 but for the DW phases.

https://doi.org/10.5194/egusphere-2026-2856
Preprint. Discussion started: 5 June 2026

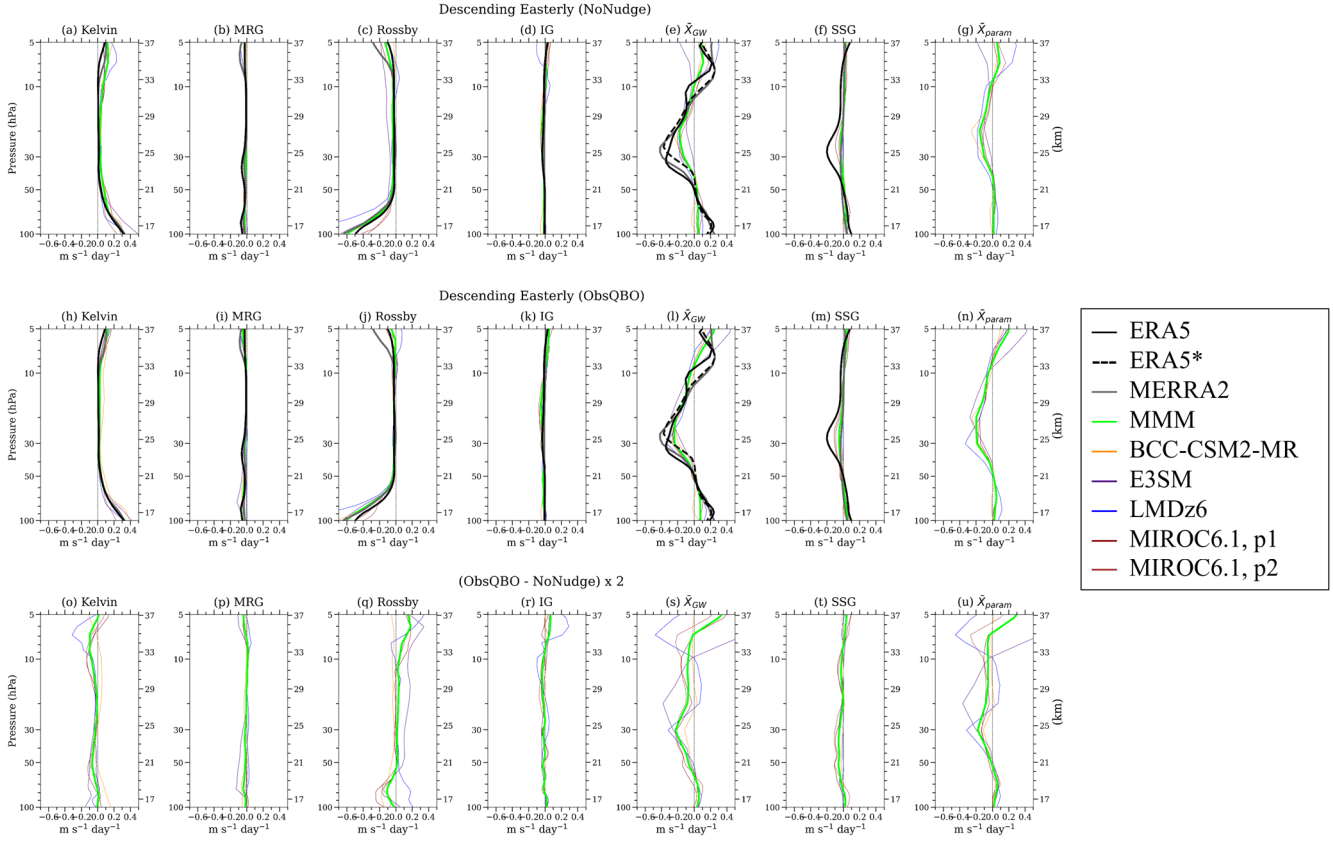

Figure 13: Same as Fig. 10 but for the DE phases.

Figure 14 illustrates the equatorial wave forcing at 10, 30, and 50 hPa, summarizing the results presented in Figures 10–13. The characteristics of Kelvin wave forcing highly depend on the QBO phase. During the WQBO phase, Kelvin waves provide eastward forcing necessary for the downward propagation of the WQBO. While the Kelvin wave forcing at 30 hPa is stronger in ObsQBO than that in NoNudge experiments, its magnitude remains insufficient compared to the reanalyses. During the EQBO phase, Kelvin wave forcing is minimal in the mid-to-lower stratosphere, whereas at 10 hPa, it provides the strongest eastward forcing among all planetary waves. In the ObsQBO experiments, the wave forcing of Kelvin waves and GWs at 10 hPa is overestimated relative to the reanalyses during the EQBO phase. Rossby waves provide westward forcing in all QBO phases. Despite their relatively small magnitude, Rossby waves provide the second-strongest westward forcing at 10 hPa during WQBO, following GWs, potentially contributing to the weakening of the WQBO and the onset of the easterly winds. The contributions of MRG and IG wave forcings are relatively minor.

https://doi.org/10.5194/egusphere-2026-2856
Preprint. Discussion started: 5 June 2026

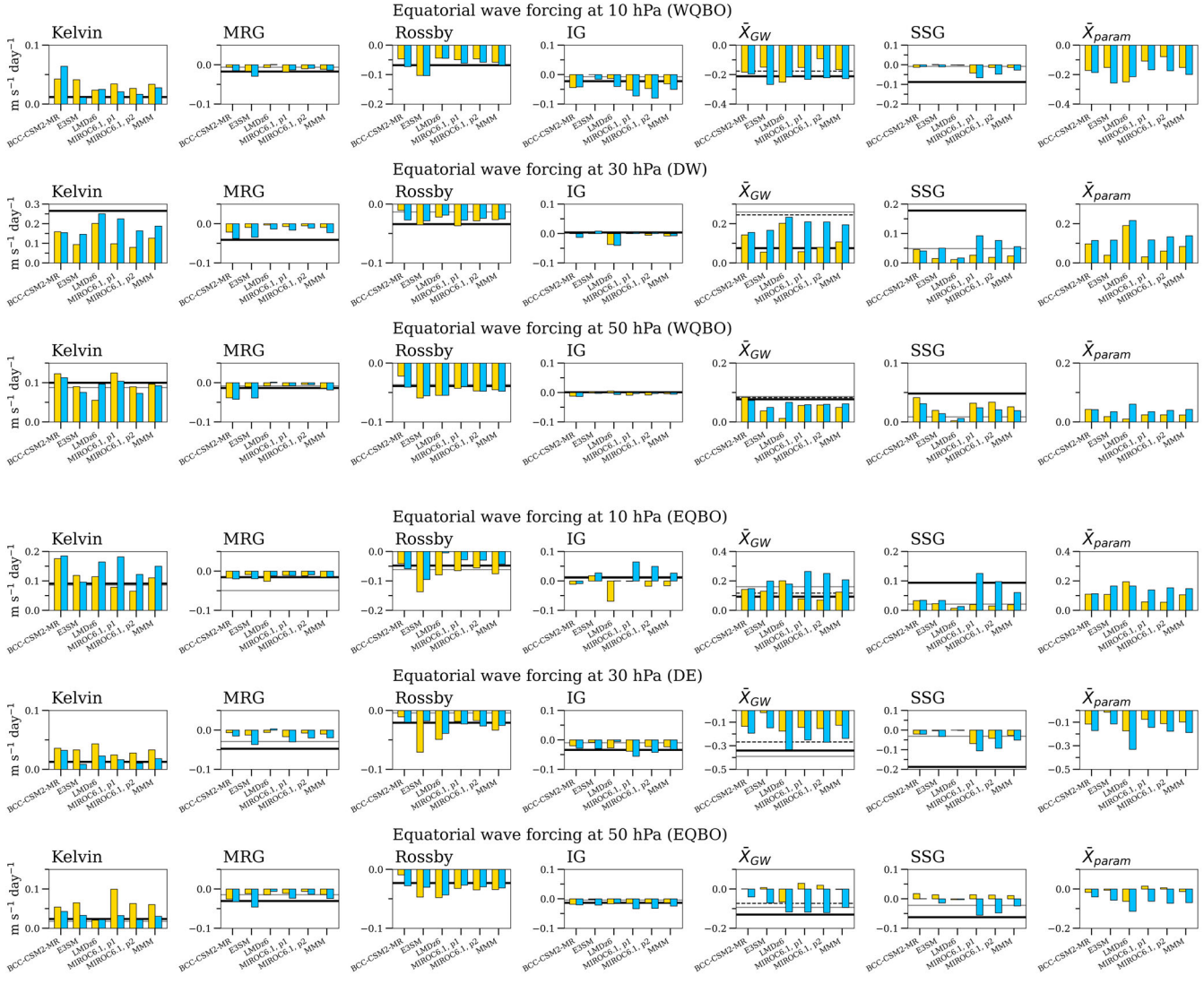

Figure 14: Composite of equatorial wave forcing averaged between 5°S and 5°N by Kelvin, MRG, Rossby, IG, GW, SSG, and parameterized GWs. The yellow and blue bars represent the NoNudge and ObsQBO experiments, respectively. The black solid lines indicate ERA5 values, gray solid lines indicate MERRA2 values, and black dashed lines indicate $\bar{X}^{*}_{GW.ref}$ of ERA5.

3.4.2 Gravity wave forcing

Following the analysis of planetary wave forcing, we examine the GW forcing in the models and compare the results with the reanalyses. Regardless of the QBO phase, ERA5 is the only case in which the contribution of SSG to GW forcing is strong, whereas in the models, the contribution of SSG is very small, and the GW forcing is dominated by $\bar{X}_{param}$ (Figs. 10–13). Because a significant portion of the momentum required for the downward propagation of the QBO is

https://doi.org/10.5194/egusphere-2026-2856
Preprint. Discussion started: 5 June 2026

provided by GWs (Fig. 7), the simulation of the QBO in the models relies strongly on non-orographic GW parameterization. The vertical structure of GW forcing in the reanalysis datasets is similar during the WQBO (Fig. 10), whereas there are quantitative differences during the EQBO (Fig. 11). This discrepancy arises from differences in vertical advection, which is used to calculate $\bar{X}_{GW.ref}$, between ERA5 and MERRA2 (Fig. S6). This is consistent with a previous study that found that inconsistency in vertical advection occurs among reanalyses (Fujiwara et al., 2022). The most pronounced discrepancy occurs between 30 and 40 hPa during the DW phase, where the GW forcing in ERA5 has a different vertical structure to that in MERRA2 (Fig. 12e). The QBO-induced downwelling observed in ERA5 overwhelms the tropical upwelling in the lower part of the WQBO (Pahlavan, Fu, et al., 2021). This results in an abrupt reversal of the sign of vertical advection (not shown), which introduces spurious distributions in $\bar{X}_{GW.ref}$. Given that the variability of $\overline{w}^*$ in ERA5 is excessive compared to observations (Ming et al., 2025), $\bar{X}_{GW.ref}$ calculated using ERA5 data could reflect uncertainty associated with $\overline{w}^*$. To assess this uncertainty, we calculate $\bar{X}^*_{GW.ref}$ using the planetary wave forcing of ERA5 and the zonal wind tendency and advection of MERRA2 (Eq. 11). The resulting $\bar{X}^*_{GW.ref}$ of ERA5 is similar to $\bar{X}_{GW.ref}$ of MERRA2, supporting the interpretation that differences in vertical advection contribute to the discrepancies in $\bar{X}_{GW.ref}$.

The vertical structure of GW forcing varies depending on the QBO phase. During the WQBO phase, GWs provide eastward forcing below 30 hPa while contributing westward forcing above 30 hPa (Figs. 10e and 10l). Above 30 hPa, the magnitudes of $\bar{X}_{GW}$ in NoNudge are comparable to those in the reanalyses, whereas they are underestimated below 30 hPa (Fig. 10e). In the ObsQBO experiments, GW forcing below 30 hPa increases and exhibits better agreement with the reanalyses (Fig. 10l), which results from nudging the background winds and thereby enhancing $\bar{X}_{param}$ (Fig. 10u). During the EQBO phase, most characteristics exhibit the opposite of those observed in the WQBO phase. GWs provide westward forcing below 30 hPa and eastward forcing above 30 hPa (Fig. 11e). The westward forcing in NoNudge is very weak below 30 hPa, reaching −0.13 m s^{-1} day^{-1} for LMDz6. This value is considerably smaller in magnitude than −0.21 m s^{-1} day^{-1} for ERA5. The nudging leads to an enhancement of GW forcing in the lower stratosphere (Fig. 11s). The MMM at 40 hPa increases by a factor of 3.3, from −0.04 to −0.15 m s^{-1} day^{-1} (Fig. 11l). Similar patterns are evident during the DW and DE phases: the GW forcing in the lower stratosphere is underestimated in the NoNudge experiments (Figs. 12e and 13e), and its magnitude is substantially improved when nudging is applied (Figs. 12s and 13s).

While nudging appears to improve the GW forcing of the model in the lower stratosphere, its role differs in the mid-to-upper stratosphere during the EQBO phase. In the NoNudge experiments, the $\bar{X}_{GW}$ of the models is comparable to that of the reanalyses (Fig. 11e). However, it exhibits a significantly enhanced eastward forcing in ObsQBO (Figs. 11l). This change is similar to that observed in the Kelvin wave forcing (Fig. 11o), and it is likely that the eastward wind bias is alleviated by nudging, thereby allowing more eastward-propagating waves to propagate upward and deposit momentum. These results suggest that both Kelvin and GWs provide excessive eastward forcing near 10 hPa associated with the QBO onset, and the influence of this forcing bias on the QBO is discussed in Sect. 4.1.

https://doi.org/10.5194/egusphere-2026-2856
Preprint. Discussion started: 5 June 2026

Additionally, the seasonality of GW forcing in the lower stratosphere is investigated. The periodic fluctuation of the QBO is closely related to the variability of GWs, and the large portion of the westward GW forcing can be explained by its seasonality (Kim, 2025). Figure 15 shows the seasonal variations of $\bar{X}_{GW}$ at 50 hPa and the maxima and minima of the zonal wind between 200 and 85 hPa, averaged over 5°N and 5°S. In ERA5 and MERRA2, the peaks of westward GW forcing occur in May and October (Fig. 15a), which are the months when the largest westward forcing occurs during EQBO (Fig. 15i). Such variability could be explained by the combination of the variability of the wave source and the zonal wind in the UTLS (Kim, 2025). In the NoNudge experiments, none of the models captured the seasonal variation of GW forcing (Fig. 15i). In the ObsQBO experiments, although the minimum westward GW forcing captured by the models occurs in May, it does not closely resemble that seen in the reanalyses (Fig. 15k). Because the seasonal variation of zonal winds is relatively well-reproduced in the models (Figs. 15b and 15d), these discrepancies may arise from uncertainties in GW parameterization. Most GCMs assume vertically propagating GWs, which neglects the role of the lateral propagation of GWs (Kim et al., 2024). In addition to the lack of observational constraints for NOGW parameterizations (Lott et al., 2024), uncertainties in latent heating also contribute to the uncertainty in source-dependent NOGW momentum flux (Alexander et al., 2021; Lee et al., 2022, Lee and Chun, 2025).

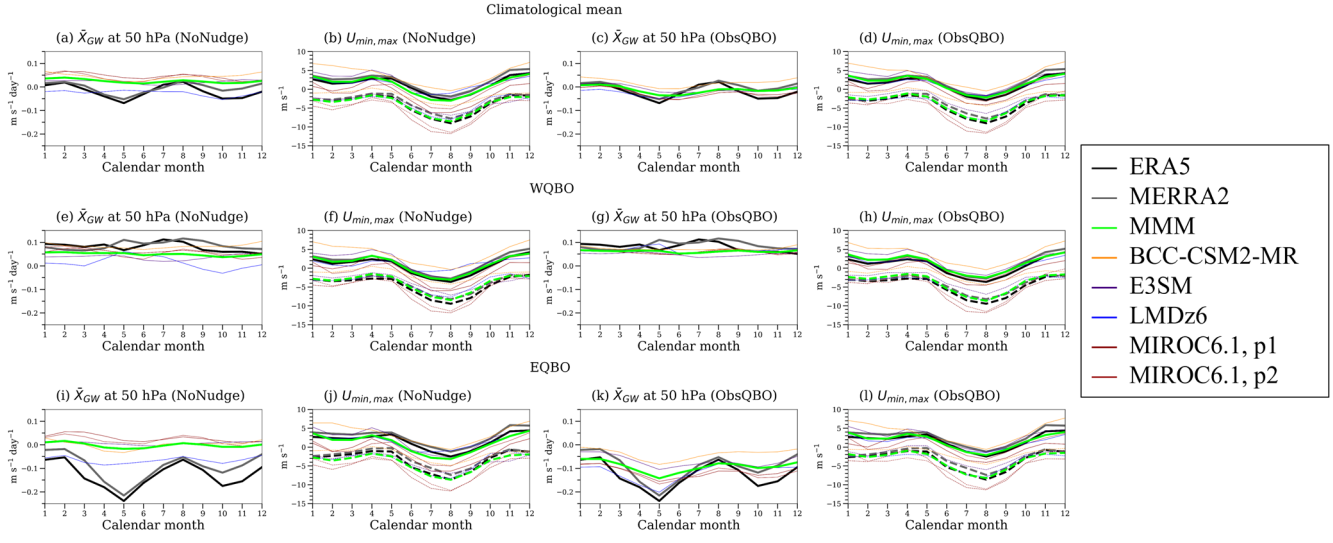

Figure 15: Seasonal cycles of (a, c, e, g, i, k) GW forcing at 50 hPa and (b, d, f, h, j, l) zonal wind maxima (solid lines) and minima (dashed lines) between 200 and 85 hPa, averaged between 5°N and 5°S, as a function of calendar month. The panels show the (top) climatological mean, (middle) composite of the WQBO phase, and (bottom) composite of the EQBO phase. The green lines denote the MMM.

https://doi.org/10.5194/egusphere-2026-2856
Preprint. Discussion started: 5 June 2026

4 Discussion

4.1 Impact of equatorial wave forcing biases on QBO biases

Equatorial wave forcing biases may affect QBO biases because wave forcing is the primary driver of the QBO. One of the major biases in wave forcing identified in this study is that Kelvin and gravity waves in ObsQBO experiments provide excessive eastward forcing in the mid-to-upper stratosphere in GCMs (Figs. 11h and 11l). To investigate their impacts on the QBO, further analysis is conducted. Figure 16 presents the composite of TEM components at 10 hPa in the −6 to +6 months lag period with respect to the occurrence of the onset of westerly and easterly winds at 10 hPa. When the onset of the easterly wind occurs, the TEM components of QBOi models in ObsQBO generally capture the characteristics of ERA5, although individual models diverge in their equatorial wave forcing (Figs. 16m–16p). By contrast, the models exhibit systematic biases during the onset of the westerly wind. The MMM of advection during onset (lag = 0) is −0.1 m s^{-1} day^{-1}, which is slightly lower than 0.0 m s^{-1} day^{-1} in ERA5 (Figs. 16c and 16g), but wave forcing in the models is generally biased eastward compared to ERA5 (Figs. 16d and 16h). Specifically, the equatorial wave forcing in the models ranges from 0.16 to 0.87 m s^{-1} day^{-1} in ObsQBO, and all models except EC-Earth3 exhibit excessive eastward forcing compared to 0.25 m s^{-1} day^{-1} in ERA5 (Fig. 16h). The correlation coefficient between eastward forcing and the WQBO amplitude is 0.8 (Fig. S8), suggesting that the eastward wind bias observed in the QBO simulations is likely to originate from an excessive eastward wave forcing in the mid-to-upper stratosphere.

https://doi.org/10.5194/egusphere-2026-2856
Preprint. Discussion started: 5 June 2026

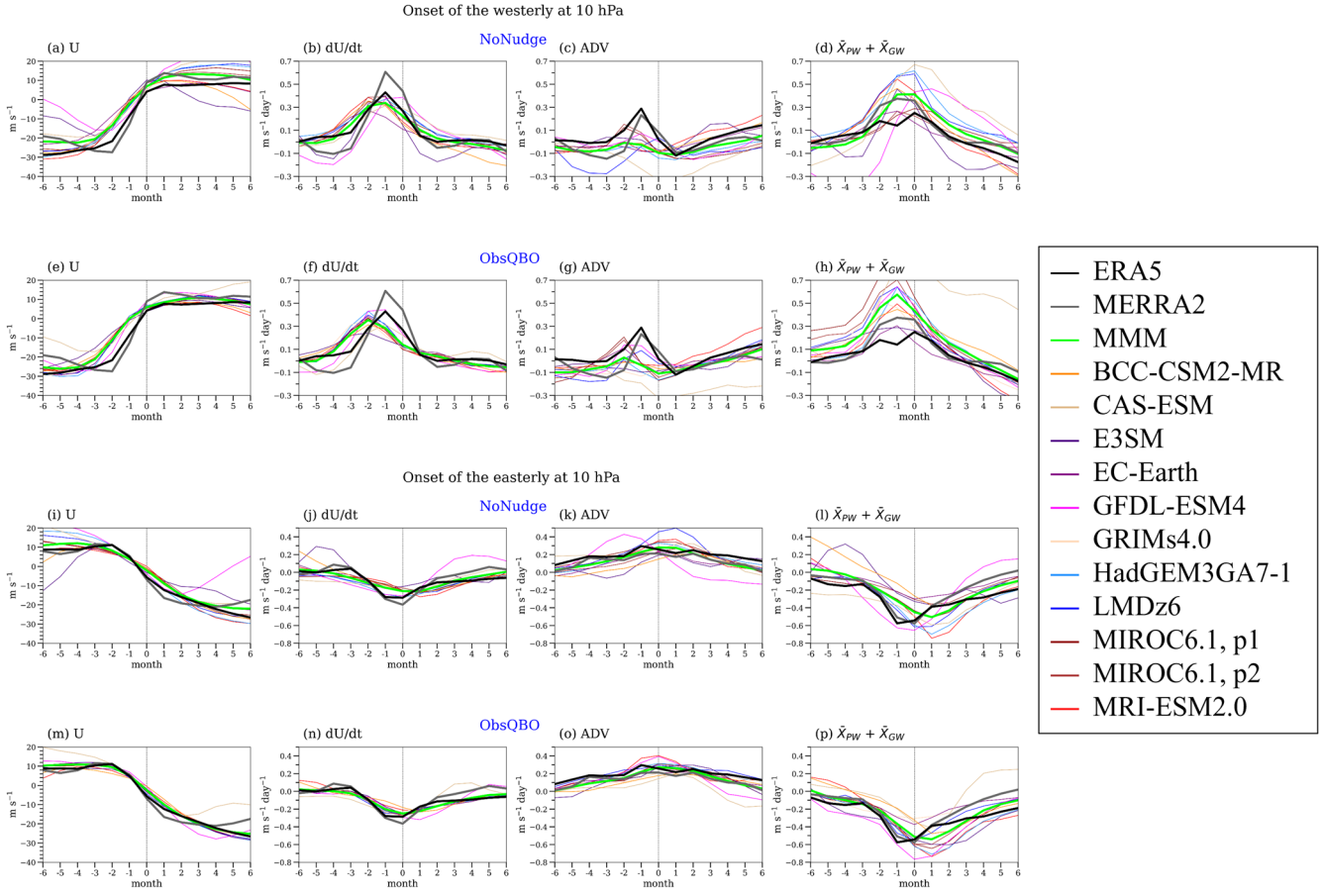

Figure 16: Composite evolution relative to the onset of the (top) westerly and (bottom) easterly winds at 10 hPa. In each panel, the month labeled "0" denotes the time when the zonal wind at 10 hPa averaged between 5°N and 5°S changes from easterly to westerly (top) and from westerly to easterly (bottom). Each column represents the TEM components: zonal wind, time tendency of zonal wind, time tendency of zonal wind caused by advection, and equatorial wave forcing, which is the sum of resolved wave forcing and parameterized GW forcing.

https://doi.org/10.5194/egusphere-2026-2856
Preprint. Discussion started: 5 June 2026

Another common bias identified across the models is that the required wave forcing to drive the QBO in the lower stratosphere is insufficient in NoNudge experiments (Figs. 8d–e and 9d–e). We investigate whether this lack of wave forcing is directly linked to the underestimation of the QBO amplitude at 50 hPa (Fig. 17). In the NoNudge experiments, the wave forcing averaged between 30 and 50 hPa (WF_{W30-50}) is positively correlated (0.92) with the amplitude at 50 hPa (A_{W50}) during the WQBO phase (Fig. 17b), whereas the WF_{E30-50} is negatively correlated (−0.75) with the A_{E50} during the EQBO phase (Fig. 17e). Wave forcing biases appear to be strongly coupled with QBO amplitude biases in the lower stratosphere. However, these correlations alone are insufficient to demonstrate that the stronger wave forcing leads to a larger A_{50}. Larger QBO amplitudes are associated with strong vertical wind shear, which may in turn facilitate enhanced wave forcing. This implies that QBO amplitude biases could also lead to wave forcing biases. Therefore, these results are insufficient to distinguish between cause and effect. The correlations between WF_{30-50} in the ObsQBO and A_{50} in the NoNudge are relatively weaker than those between WF_{30-50} and A_{50} in the NoNudge (Figs. 17c and 17f), and the correlations are not stronger than those between the QBO amplitudes at 10 hPa and 50 hPa in the NoNudge experiments (Figs. 17a and 17d). The link between these two levels is consistent with the downward propagation of the QBO. Given the significant role of wave forcing in the onset of the QBO at 10 hPa (Fig. 16), this suggests that the bias in the QBO amplitude at 50 hPa is likely associated with the cumulative effects of wave forcing biases extending from the lower to the upper equatorial stratosphere.

Another notable feature is that the type of NOGW parameterization influences the correlation between WF_{30-50} in the ObsQBO and A_{50}. In models with fixed-source NOGW parameterization, the magnitude of the correlation between WF_{30-50} and A_{50} is less than 0.1 (Figs. S9c and S9f). Conversely, in models with source-dependent parameterization, models with stronger wave forcing tend to exhibit larger A_{50} (Figs. S10c and S10f). For the NOGW parameterization, the GWD in the equatorial region is primarily determined by both the dynamical filtering by the background wind and the wave source type (Lott et al., 2024). For the fixed-source NOGW parameterization, since the source is fixed and the background wind is constrained to ERA5 through nudging, the explicit relationship between the GWD bias of the model and the A_{50} bias could be eliminated. However, because the sample size for each group is relatively small, these results should be interpreted with caution.

https://doi.org/10.5194/egusphere-2026-2856
Preprint. Discussion started: 5 June 2026

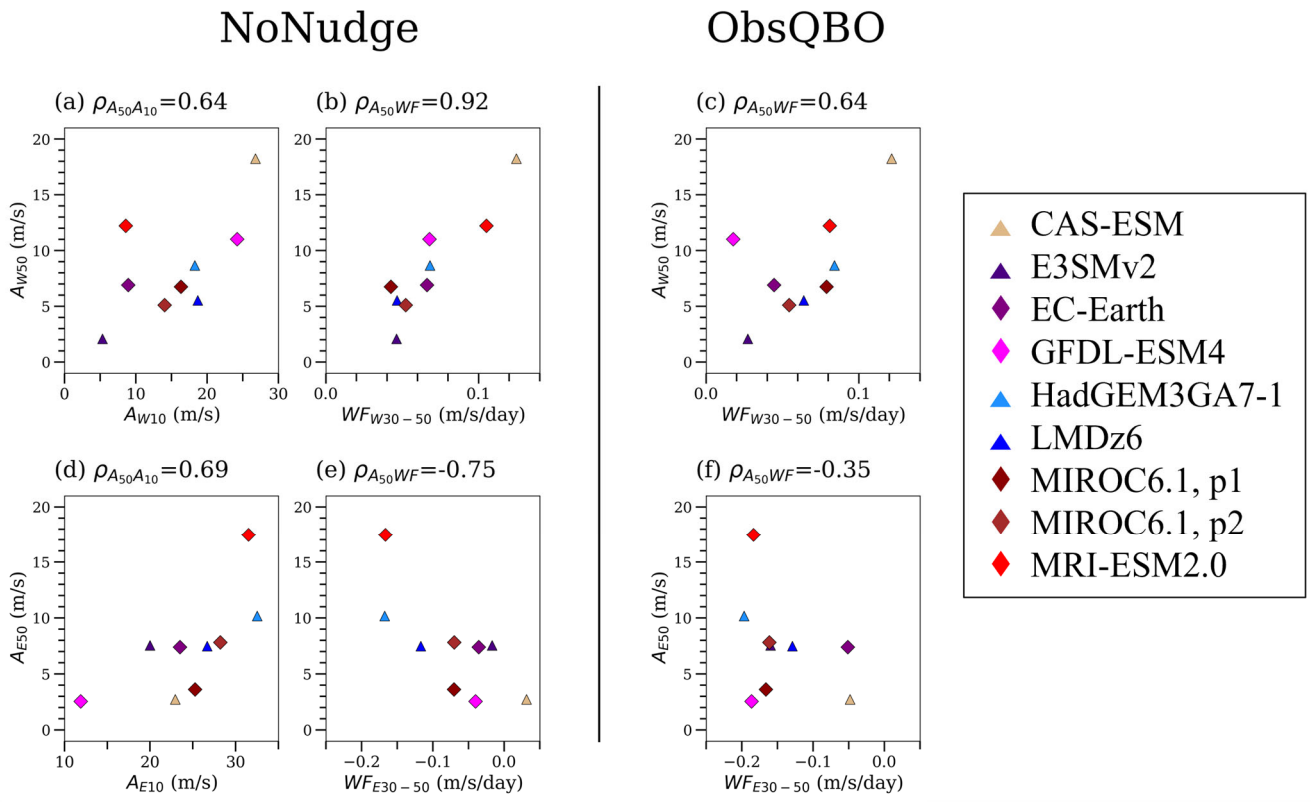

Figure 17: Scatter plots depicting the relationship between the QBO amplitudes at 50 hPa and 10 hPa (A_{50} and A_{10}) in the NoNudge experiments, and the wave forcing averaged between 30 and 50 hPa (WF_{30-50}). The subscripts W and E denote the WQBO and EQBO phases, respectively. The amplitudes are listed in Table 2. The y-axis in the top panels show the WQBO amplitudes at 50 hPa (A_{W50}), and the y-axis in the bottom panels show the EQBO amplitudes at 50 hPa (A_{E50}). The x-axis in the panels (b, e) and (c, f) represents WF_{30-50} in NoNudge and ObsQBO experiments, respectively. Wave forcing is defined as the sum of resolved wave forcing and parameterized GW forcing. Different symbols represent different types of NOGW sources. Triangles represent the source-dependent gravity wave parameterization, and diamonds represent the fixed-source gravity wave parameterization. Statistical significance exceeds 90% when ρ is larger than 0.58. BCC-CSM2-MR was excluded because its nudged QBO amplitude at 50 hPa is more than $2\sigma_{ref}$ smaller than that in ERA5 (Fig. 2).

4.2 QBO disruption

This study uses a 42-year dataset spanning from 1979 to 2020, which includes the 2015/16 and 2019/20 QBO disruption events. None of the models simulate these events in their NoNudge experiments (Fig. S1), and the inclusion of these events could contribute to the lower performance scores of the QBO metrics in the NoNudge experiments (Fig. S2). When the analysis period is restricted to 1979–2009, consistent with Bushell et al. (2022), the QBO metrics improve

https://doi.org/10.5194/egusphere-2026-2856
Preprint. Discussion started: 5 June 2026

compared to those calculated using the full period (not shown). Previous studies demonstrated that the primary source of QBO disruptions is anomalous wave forcing (Kang et al., 2020a; Kang and Chun, 2021; Kang et al., 2022). The nudging experiment is a useful tool for examining the wave dynamics during QBO disruptions (Wang et al., 2025), and it could also help identify potential reasons why current models fail to reproduce these events. However, a detailed diagnosis of these deficiencies is beyond the scope of this study and is left for future investigation.

5 Summary and conclusion

In this study, we analyzed the resolved and parameterized equatorial wave forcing using 11 QBOi models covering the 42-year period from 1979 to 2020. The ObsQBO experiments, in which nudging is used to bias-correct the QBO zonal winds, effectively mitigate the equatorial stratospheric wind biases found in the NoNudge experiments and exhibit improved QBO period, amplitude, and vertical and latitudinal extent. The application of nudging limited to the equatorial stratosphere has a negligible effect on the PSD of precipitation, which is linked to the tropospheric wave sources, indicating that bias correction of the equatorial stratospheric winds has no substantial impact on tropical precipitation in these models. Through the TEM momentum budget analysis, it is evident that the models lack sufficient forcing for realistic downward propagation of the QBO in the lower stratosphere. Because the zonal wind tendency caused by advection in the nudged simulations aligns closely with ERA5 in the multi-model mean, insufficient wave forcing is implicated as the primary cause of weak QBO amplitude in the lower stratosphere in the QBOi models, particularly in the EQBO phase.

In reanalyses, the downward propagation of the QBO is mainly driven by Kelvin and GWs during the WQBO phase and by GWs during the EQBO phase, whereas the models in the NoNudge experiments exhibit insufficient wave forcing of both Kelvin and GWs in the lower stratosphere. When nudging is applied, the wave forcing in the lower stratosphere increases. This suggests that the weak wave forcing in the models is partly a result of weak vertical wind shear, which prevents the waves from being dissipated at this level. However, it is notable that even when background winds are realistic (due to the nudging), wave driving in descending westerly and easterly QBO shear zones is still underestimated compared to the reanalyses. These findings indicate that the models inherently struggle to generate the wave forcing required for the downward propagation of the QBO. Another impact of nudging is that models exhibit excessive eastward forcing for both Kelvin and GWs during the EQBO near 10 hPa. Excessive eastward forcing likely leads to an overestimation of the WQBO amplitude, potentially contributing to the eastward wind bias near 10 hPa commonly found in QBO-resolving models. Furthermore, QBO amplitude biases at 10 hPa could influence the QBO structure in the lower stratosphere through downward propagation. Therefore, these results highlight the need for improved physical realism in NOGW parameterizations, together with a realistic representation of equatorial planetary waves in the equatorial stratosphere.

https://doi.org/10.5194/egusphere-2026-2856
Preprint. Discussion started: 5 June 2026

Data availability

ERA5 data are available at https://doi.org/10.24381/cds.143582cf (Hersbach et al., 2017). MERRA2 data are available at https://doi.org/10.5067/WWQSXQ8IVFW8 (Global Modeling and Assimilation Office (GMAO), 2015). GPCP data are available at https://doi.org/10.5067/MEASURES/GPCP/DATA307 (Huffman et al., 2025). The QBOi phase 2 model outputs are hosted by the NERC Centre for Environmental Data Analysis (CEDA), UK.

Author contributions

HKL performed conceptualization, data curation, formal analysis, investigation, visualization, and writing (original draft preparation, review and editing). JAA performed conceptualization, formal analysis, investigation, project administration, supervision, and writing (review and editing). HYC performed formal analysis, funding acquisition, supervision, and writing (review and editing). SW, FL, ZC, YL, QT, JX, DCH, SWS, PD, FS, PL, MBA, NB, AMJ, JRK, SO, HN, KY provided model output and reviewed and edited the manuscript. JAA, NB, YK, SO, and JR designed the QBOi phase 2 experiments.

Competing interests

JAA serves as co-editor for the special issue to which this paper belongs. The remaining authors declare that they have no conflict of interest.

Disclaimer

Publisher's note: Copernicus Publications remains neutral with regard to jurisdictional claims made in the text, published maps, institutional affiliations, or any other geographical representation in this paper. While Copernicus Publications makes every effort to include appropriate place names, the final responsibility lies with the authors. Views expressed in the text are those of the authors and do not necessarily reflect the views of the publisher.

Acknowledgements

We acknowledge the scientific guidance of the World Climate Research Programme (WCRP) for helping motivate this work, coordinated under the framework of the Atmospheric Processes And their Role in Climate (APARC) QBO initiative (QBOi) phase-2 led by JAA, NB, YK, SO, and JR. FS thanks Paolo Davini for support in setting up the simulations of the EC-Earth3 model and acknowledges computing and archive resources provided by an ECMWF Special Project.

https://doi.org/10.5194/egusphere-2026-2856
Preprint. Discussion started: 5 June 2026

Financial support

This work was supported by the National Research Foundation of Korea (NRF) grant funded by the Korea government (MSIT) (RS-2025-19623005). QT and JX acknowledge support from the E3SM project, funded by the U.S. Department of Energy (DOE), Office of Science, Office of Biological and Environmental Research (BER) through the Earth System Model Development (ESMD) program area. QT acknowledges grant support from the U.S. DOE BER's Regional and Global Model Analysis (RGMA) program via SCW1813. Lawrence Livermore National Laboratory is operated by Lawrence Livermore National Security, LLC, for the U.S. DOE, National Nuclear Security Administration under Contract DE-AC52-07NA27344. SW was supported by JSPS KAKENHI Grant Number JP26K00773 and the MEXT Program for Advanced Studies of Climate Change Projection (SENTAN) Grant Number JPMXD0722681344. MIROC6.1 simulations were performed using the Earth Simulator at JAMSTEC.

References

Alexander, M. J., Liu, C. C., Bacmeister, J., Bramberger, M., Hertzog, A., and Richter, J. H.: Observational validation of parameterized gravity waves from tropical convection in the Whole Atmosphere Community Climate Model, J. Geophys. Res.-Atmos., 126, https://doi.org/10.1029/2020JD033954, 2021.

Andrews, D. G., Leovy, C. B., and Holton, J. R.: Middle atmosphere dynamics, Academic press, 1987.

Anstey, J. A., Simpson, I. R., Richter, J. H., Naoe, H., Taguchi, M., Serva, F., Gray, L. J., Butchart, N., Hamilton, K., Osprey, S., Bellprat, O., Braesicke, P., Bushell, A. C., Cagnazzo, C., Chen, C. C., Chun, H.-Y., Garcia, R. R., Holt, L., Kawatani, Y., Kerzenmacher, T., Kim, Y. H., Lott, F., McLandress, C., Scinocca, J., Stockdale, T. N., Versick, S., Watanabe, S., Yoshida, K., and Yukimoto, S.: Teleconnections of the quasi-biennial oscillation in a multi-model ensemble of QBO-resolving models, Q. J. Roy. Meteorol. Soc., 148, 1568–1592, https://doi.org/10.1002/qj.4048, 2022.

Anstey, J. A., Butchart, N., Osprey, S., Kawatani, Y., Hamilton, K., Richter, J. H., Stockdale, T., Andrews, M. B., Chai, Z., Davini, P., Hong, D.-C., Huang, K., Jaison, A. M., Kerzenmacher, T., Knight, J. R., Lin, P., Lott, F., Lu, Y., Naoe, H., Serva, F., Simpson, I., Son, S.-W., Tang, Q., Watanabe, S., Xie, J., and Yoshida, K.: Experiment design, nudging protocol, and models participating in Phase 2 of the APARC Quasi-Biennial Oscillation initiative (QBOi), EGUsphere, 2026, 1–38, https://doi.org/10.5194/egusphere-2026-1165, 2026.

Andrews, M. B., Knight, J. R., Scaife, A. A., and Wicker, W.: Influence of the Quasi-Biennial Oscillation on tropical convection and its teleconnection to the midlatitudes in boreal winter, Q. J. Roy. Meteorol. Soc., 150, 2510–2521, https://doi.org/10.1002/qj.4721, 2024.

Baldwin, M. P., Gray, L. J., Dunkerton, T. J., Hamilton, K., Haynes, P. H., Randel, W. J., Holton, J. R., Alexander, M. J., Hirota, I., Horinouchi, T., Jones, D. B. A., Kinnersley, J. S., Marquardt, C., Sato, K., and Takahashi, M.: The quasi-biennial oscillation, Rev. Geophys., 39, 179–229, https://doi.org/10.1029/1999RG000073, 2001.

https://doi.org/10.5194/egusphere-2026-2856
Preprint. Discussion started: 5 June 2026

Bushell, A. C., Anstey, J. A., Butchart, N., Kawatani, Y., Osprey, S. M., Richter, J. H., Serva, F., Braesicke, P., Cagnazzo, C., Chen, C. C., Chun, H.-Y., Garcia, R. R., Gray, L. J., Hamilton, K., Kerzenmacher, T., Kim, Y.-H., Lott, F., McLandress, C., Naoe, H., Scinocca, J., Smith, A. K., Stockdale, T. N., Versick, S., Watanabe, S., Yoshida, K., and Yukimoto, S.: Evaluation of the quasi-biennial oscillation in global climate models for the SPARC QBO-initiative, Q. J. Roy. Meteorol. Soc., 148, 1459–1489, https://doi.org/10.1002/qj.3765, 2022.

Chien, M.-T. and Kim, D.: Representation of the convectively coupled Kelvin waves in modern reanalysis products, J. Atmos. Sci., 80, https://doi.org/10.1175/JAS-D-22-0067.1, 2023.

Dunkerton, T. J. and Delisi, D. P.: Climatology of the equatorial lower stratosphere, J. Atmos. Sci., 42, 376–396, https://doi.org/https://doi.org/10.1175/1520-0469(1985)042<0376:COTELS>2.0.CO;2, 1985.

Ern, M., Diallo, M., Preusse, P., Mlynczak, M. G., Schwartz, M. J., Wu, Q., and Riese, M.: The semiannual oscillation (SAO) in the tropical middle atmosphere and its gravity wave driving in reanalyses and satellite observations, Atmos. Chem. Phys., 21, 13763–13795, https://doi.org/10.5194/acp-21-13763-2021, 2021.

Ern, M., Cho, H.-K., Preusse, P., and Eckermann, S. D.: Properties of the average distribution of equatorial Kelvin waves investigated with the GROGRAT ray tracer, Atmos. Chem. Phys., 9, 7973–7995, https://doi.org/10.5194/acp-9-7973-2009, 2009.

Fujiwara, M., Manney, G. L., Gray, L. J., and Wright, J. S.: SPARC Reanalysis Intercomparison Project (S-RIP) Final Report, https://doi.org/10.17874/800dee57d13, 2022.

Garcia, R. R. and Richter, J. H.: On the momentum budget of the quasi-biennial oscillation in the whole atmosphere community climate model, J. Atmos. Sci., 76, 69–87, https://doi.org/10.1175/JAS-D-18-0088.1, 2019.

García-Franco, J. L., Gray, L. J., Osprey, S., Jaison, A. M., Chadwick, R., and Lin, J.: Understanding the mechanisms for tropical surface impacts of the quasi-biennial oscillation (QBO), J. Geophys. Res.-Atmos., 128, https://doi.org/10.1029/2023JD038474, 2023.

Garfinkel, C. I., Shaw, T. A., Hartmann, D. L., and Waugh, D. W.: Does the Holton-Tan mechanism explain how the quasi-biennial oscillation modulates the Arctic polar vortex?, J. Atmos. Sci., 69, 1713–1733, https://doi.org/10.1175/JAS-D-11-0209.1, 2012.

Garfinkel, C. I., Schwartz, C., Domeisen, D. I. V., Son, S. W., Butler, A. H., and White, I. P.: Extratropical atmospheric predictability from the quasi-biennial oscillation in subseasonal forecast models, J. Geophys. Res.-Atmos., 123, 7855–7866, https://doi.org/10.1029/2018JD028724, 2018.

Gelaro, R., McCarty, W., Suárez, M. J., Todling, R., Molod, A., Takacs, L., Randles, C. A., Darmenov, A., Bosilovich, M. G., Reichle, R., Wargan, K., Coy, L., Cullather, R., Draper, C., Akella, S., Buchard, V., Conaty, A., da Silva, A. M., Gu, W., Kim, G. K., Koster, R., Lucchesi, R., Merkova, D., Nielsen, J. E., Partyka, G., Pawson, S., Putman, W., Rienecker, M., Schubert, S. D., Sienkiewicz, M., and Zhao, B.: The modern-era retrospective analysis for research and applications, version 2 (MERRA-2), J Clim, 30, 5419–5454, https://doi.org/10.1175/JCLI-D-16-0758.1, 2017.

https://doi.org/10.5194/egusphere-2026-2856
Preprint. Discussion started: 5 June 2026

Global Modeling and Assimilation Office (GMAO): MERRA-2 inst3_3d_asm_Nv: 3d,3-Hourly,Instantaneous,Model-Level,Assimilation,Assimilated Meteorological Fields V5.12.4, Greenbelt, MD, USA, Goddard Earth Sciences Data and Information Services Center (GES DISC), https://doi.org/10.5067/WWQSXQ8IVFW8, 2015.

Golaz, J.-C., Van Roekel, L. P., Zheng, X., Roberts, A. F., Wolfe, J. D., Lin, W., Bradley, A. M., Tang, Q., Maltrud, M. E., Forsyth, R. M., Zhang, C., Zhou, T., Zhang, K., Zender, C. S., Wu, M., Wang, H., Turner, A. K., Singh, B., Richter, J. H., Qin, Y., Petersen, M. R., Mametjanov, A., Ma, P.-L., Larson, V. E., Krishna, J., Keen, N. D., Jeffery, N., Hunke, E. C., Hannah, W. M., Guba, O., Griffin, B. M., Feng, Y., Engwirda, D., Di Vittorio, A. V., Dang, C., Conlon, L. M., Chen, C.-C.-J., Brunke, M. A., Bisht, G., Benedict, J. J., Asay-Davis, X. S., Zhang, Y., Zhang, M., Zeng, X., Xie, S., Wolfram, P. J., Vo, T., Veneziani, M., Tesfa, T. K., Sreepathi, S., Salinger, A. G., Reeves Eyre, J. E. J., Prather, M. J., Mahajan, S., Li, Q., Jones, P. W., Jacob, R. L., Huebler, G. W., Huang, X., Hillman, B. R., Harrop, B. E., Foucar, J. G., Fang, Y., Comeau, D. S., Caldwell, P. M., Bartoletti, T., Balaguru, K., Taylor, M. A., McCoy, R. B., Leung, L. R., and Bader, D. C.: The DOE E3SM model version 2: Overview of the physical model and initial model evaluation, J. Adv. Model. Earth Syst., 14, e2022MS003156, https://doi.org/https://doi.org/10.1029/2022MS003156, 2022.

Hersbach, H., Bell, B., Berrisford, P., Hirahara, S., Horányi, A., Muñoz-Sabater, J., Nicolas, J., Peubey C., Radu, R., Schepers, D., Simmons, A., Soci, C., Abdalla, S., Abellan, X., Balsamo, G., Bechtold, P., Biavati, G., Bidlot, J., Bonavita, M., De Chiara, G., Dahlgren, P., Dee, D., Diamantakis, M., Dragani, R., Flemming, J., Forbes, R., Fuentes, M., Geer, A., Haimberger, L., Healy, S., Hogan, R. J., Hólm, E., Janisková, M., Keeley, S., Laloyaux, P., Lopez, P., Lupu, C., Radnoti, G., de Rosnay, P., Rozum, I., Vamborg, F., Villaume, S., and Thépaut, J.-N.: Complete ERA5 from 1940: Fifth generation of ECMWF atmospheric reanalyses of the global climate. Copernicus Climate Change Service (C3S) Data Store (CDS), https://doi.org/https://doi.org/10.24381/cds.143582cf, 2017.

Hersbach, H., Bell, B., Berrisford, P., Hirahara, S., Horányi, A., Muñoz-Sabater, J., Nicolas, J., Peubey, C., Radu, R., Schepers, D., Simmons, A., Soci, C., Abdalla, S., Abellan, X., Balsamo, G., Bechtold, P., Biavati, G., Bidlot, J., Bonavita, M., De Chiara, G., Dahlgren, P., Dee, D., Diamantakis, M., Dragani, R., Flemming, J., Forbes, R., Fuentes, M., Geer, A., Haimberger, L., Healy, S., Hogan, R. J., Hólm, E., Janisková, M., Keeley, S., Laloyaux, P., Lopez, P., Lupu, C., Radnoti, G., de Rosnay, P., Rozum, I., Vamborg, F., Villaume, S., and Thépaut, J. N.: The ERA5 global reanalysis, Q. J. Roy. Meteorol. Soc., 146, 1999–2049, https://doi.org/10.1002/qj.3803, 2020.

Holt, L. A., Lott, F., Garcia, R. R., Kiladis, G. N., Cheng, Y. M., Anstey, J. A., Braesicke, P., Bushell, A. C., Butchart, N., Cagnazzo, C., Chen, C. C., Chun, H.-Y., Kawatani, Y., Kerzenmacher, T., Kim, Y.-H., McLandress, C., Naoe, H., Osprey, S., Richter, J. H., Scaife, A. A., Scinocca, J., Serva, F., Versick, S., Watanabe, S., Yoshida, K., and Yukimoto, S.: An evaluation of tropical waves and wave forcing of the QBO in the QBOi models, Q. J. Roy. Meteorol. Soc., 148, 1541–1567, https://doi.org/10.1002/qj.3827, 2022.

Holton, J. R. and Lindzen, R. S.: An updated theory for the quasi-biennial cycle of the tropical stratosphere, J. Atmos. Sci., 29, https://doi.org/10.1175/1520-0469(1972)029<1076:AUTFTQ>2.0.CO;2, 1972.

https://doi.org/10.5194/egusphere-2026-2856
Preprint. Discussion started: 5 June 2026

Holton, J. R. and Tan, H.-C.: The influence of the equatorial quasi-biennial oscillationon the global circulation at 50 mb, J. Atmos. Sci., 37, https://doi.org/10.1175/1520-0469(1980)037<2200:TIOTEQ>2.0.CO;2, 1980.

Huffman, G. J., Behrangi, A., Bolvin, D. T., and Nelkin, E. J.: GPCP Version 3.3 Daily Precipitation Data Set, Greenbelt, Maryland, USA, Goddard Earth Sciences Data and Information Services Center (GES DISC), https://doi.org/10.5067/MEASURES/GPCP/DATA307, 2025.

Jin, D., Kim, D., Son, S. W., and Oreopoulos, L.: QBO deepens MJO convection, Nat. Commun., 14, https://doi.org/10.1038/s41467-023-39465-7, 2023.

Kang, M.-J. and Chun, H.-Y.: Contributions of equatorial waves and small-scale convective gravity waves to the 2019/20 quasi-biennial oscillation (QBO) disruption, Atmos. Chem. Phys., 21, 9839–9857, https://doi.org/10.5194/acp-21-9839-2021, 2021.

Kang, M.-J., Chun, H.-Y., and Garcia, R. R.: Role of equatorial waves and convective gravity waves in the 2015/16 quasi-biennial oscillation disruption, Atmos. Chem. Phys., 20, 14669–14693, https://doi.org/10.5194/acp-20-14669-2020, 2020a.

Kang, M.-J., Chun, H.-Y., Kim, Y.-H., Preusse, P., and Ern, M.: Momentum flux of convective gravity waves derived from an offline gravity wave parameterization. Part II: Impacts on the quasi-biennial oscillation, J. Atmos. Sci., 75, https://doi.org/10.1175/JAS-D-18-0094.1, 2018.

Kang, M.-J., Chun, H.-Y., and Song, B.-G.: Contributions of convective and orographic gravity waves to the Brewer-Dobson circulation estimated from NCEP CFSR, J. Atmos. Sci., 77, https://doi.org/10.1175/JAS-D-19-0177.1, 2020b.

Kang, M.-J., Chun, H.-Y., Son, S.-W., Garcia, R. R., An, S.-I., and Park, S.-H.: Role of tropical lower stratosphere winds in quasi-biennial oscillation disruptions, Sci. Adv., 7229 pp., 2022.

Kim, Y.-H. and Chun, H.-Y.: Contributions of equatorial wave modes and parameterized gravity waves to the tropical QBO in HadGEM2, J. Geophys. Res.-Atmos., 120, 1065–1090, https://doi.org/10.1002/2014JD022174, 2015a.

Kim, Y.-H. and Chun, H.-Y.: Momentum forcing of the quasi-biennial oscillation by equatorial waves in recent reanalyses, Atmos. Chem. Phys., 15, 6577–6587, https://doi.org/10.5194/acp-15-6577-2015, 2015b.

Kim, Y.-H.: Explaining the period fluctuation of the quasi-biennial oscillation, Atmos. Chem. Phys., 25, 5647–5664, https://doi.org/10.5194/acp-25-5647-2025, 2025.

Kim, Y.-H., Voelker, G. S., Bölöni, G., Zängl, G., and Achatz, U.: Crucial role of obliquely propagating gravity waves in the quasi-biennial oscillation dynamics, Atmos. Chem. Phys., 24, 3297–3308, https://doi.org/10.5194/acp-24-3297-2024, 2024.

Lee, H.-K., Kang, M.-J., Chun, H.-Y., Kim, D., and Shin, D.-B: Characteristics of latent heating rate from GPM and convective gravity wave momentum flux calculated using the GPM data, J. Geophys. Res.-Atmos., 127, https://doi.org/10.1029/2022JD037003, 2022.

https://doi.org/10.5194/egusphere-2026-2856
Preprint. Discussion started: 5 June 2026

Lee, H.-K., Chun, H.-Y., Richter, J. H., Simpson, I. R., and Garcia, R. R.: Contributions of parameterized gravity waves and resolved equatorial waves to the QBO period in a future climate of CESM2, J. Geophys. Res.-Atmos., 129, https://doi.org/10.1029/2024JD040744, 2024.

Lee, H.-K., and Chun, H.-Y.: Estimations of latent heating rate using ERA5 reanalysis data and comparison with GPM, Geophys. Res. Lett., 52, https://doi.org/10.1029/2024GL113421, 2025.

Lee, J.-H., Kang, M.-J., and Chun, H.-Y.: Differences in the tropical convective activities at the opposite phases of the quasi-biennial oscillation, Asia Pac. J. Atmos. Sci., 55, 317–336, https://doi.org/10.1007/s13143-018-0096-x, 2019.

Lee, S.-H., Park, S.-H., Chien, M.-T., and Kim, D.: Simulations of convectively coupled Kelvin waves (CCKWs) with three different cumulus parameterization schemes, J. Geophys. Res.-Atmos., 130, https://doi.org/10.1029/2024JD042738, 2025.

Liess, S. and Geller, M. A.: On the relationship between QBO and distribution of tropical deep convection, J. Geophys. Res.-Atmos., 117, https://doi.org/10.1029/2011JD016317, 2012.

Lindzen, R. S. and Holton, J. R.: A theory of the quasi-biennial oscillation, J. Atmos. Sci., 25, https://doi.org/10.1175/1520-0469(1968)025<1095:ATOTQB>2.0.CO;2, 1968.

Lott, F., Denvilbutchart, S. N., Cagnazzo, C., Giorgetta, M. A., Hardiman, S. C., Manzini, E., Krismer, T., Duvel, J. P., Maury, P., Scinocca, J. F., Watanabe, S., and Yukimoto, S.: Kelvin and Rossby-gravity wave packets in the lower stratosphere of some high-top CMIP5 models, J. Geophys. Res.-Atmos., 119, 2156–2173, https://doi.org/10.1002/2013JD020797, 2014.

Lott, F., Rani, R., McLandress, C., Podglajen, A., Bushell, A., Bramberger, M., Lee, H.-K., Alexander, J., Anstey, J., Chun, H.-Y., Hertzog, A., Butchart, N., Kim, Y.-H., Kawatani, Y., Legras, B., Manzini, E., Naoe, H., Osprey, S., Plougonven, R., Pohlmann, H., Richter, J. H., Scinocca, J., García-Serrano, J., Serva, F., Stockdale, T., Versick, S., Watanabe, S., and Yoshida, K.: Comparison between non-orographic gravity-wave parameterizations used in QBOi models and Strateole 2 constant-level balloons, Q. J. Roy. Meteorol. Soc., 150, 3721–3736, https://doi.org/10.1002/qj.4793, 2024.

Mahó, S. I., Lunkeit, F., Vasylkevych, S., and Žagar, N.: The effect of barotropic instability on mixed Rossby-gravity wave variability during the QBO phases, J. Geophys. Res.-Atmos., 130, https://doi.org/10.1029/2025JD043925, 2025.

Match, A. and Fueglistaler, S.: Anomalous dynamics of QBO disruptions explained by 1D theory with external triggering, J. Atmos. Sci., 78, 373–383, https://doi.org/10.1175/JAS-D-20-0172.1, 2021.

Ming, A., Hitchcock, P., Orbe, C., and Dubé, K.: Phase and amplitude relationships between ozone, temperature, and circulation in the quasi-biennial oscillation, J. Geophys. Res.-Atmos., 130, https://doi.org/10.1029/2024JD042469, 2025.

Naoe, H., García-Franco, J. L., Park, C. H., Rodrigo, M., Palmeiro, F. M., Serva, F., Taguchi, M., Yoshida, K., Anstey, J. A., García-Serrano, J., Son, S. W., Kawatani, Y., Butchart, N., Hamilton, K., Chen, C. C., Glanville, A., Kerzenmacher, T., Lott, F., Orbe, C., Osprey, S., Park, M., Richter, J. H., Versick, S., and Watanabe, S.: QBOi El Niño–Southern

https://doi.org/10.5194/egusphere-2026-2856
Preprint. Discussion started: 5 June 2026

Oscillation experiments: teleconnections of the QBO, Weather Clim. Dynam., 6, 1419–1442, https://doi.org/10.5194/wcd-6-1419-2025, 2025.

Pahlavan, H. A., Fu, Q., Wallace, J. M., and Kiladis, G. N.: Revisiting the quasi-biennial oscillation as seen in ERA5. Part I: Description and momentum Budget, J. Atmos. Sci., 78, https://doi.org/10.1175/JAS-D-20-0248.1, 2021a.

Pahlavan, H. A., Wallace, J. M., Fu, Q., and Kiladis, G. N.: Revisiting the quasi-biennial oscillation as seen in ERA5. Part II: Evaluation of waves and wave Forcing, J. Atmos. Sci., 78, https://doi.org/10.1175/JAS-D-20-0249.1, 2021b.

Plougonven, R., de la Cámara, A., Hertzog, A., and Lott, F.: How does knowledge of atmospheric gravity waves guide their parameterizations?, Q. J. Roy. Meteorol. Soc., 146, 1529–1543, https://doi.org/10.1002/qj.3732, 2020.

Plumb, R. A. and Bell, R. C.: A model of the quasi-biennial oscillation on an equatorial beta-plane, Q. J. Roy. Meteorol. Soc., 108, 335–352, https://doi.org/10.1002/qj.49710845604, 1982.

Richter, J. H., Solomon, A., and Bacmeister, J. T.: On the simulation of the quasi-biennial oscillation in the community atmosphere model, version 5, J. Geophys. Res., 119, 3045–3062, https://doi.org/10.1002/2013JD021122, 2014.

Richter, J. H., Anstey, J. A., Butchart, N., Kawatani, Y., Meehl, G. A., Osprey, S., and Simpson, I. R.: Progress in simulating the quasi-biennial oscillation in CMIP models, J. Geophys. Res.-Atmos., 125, https://doi.org/10.1029/2019JD032362, 2020.

Richter, J. H., Butchart, N., Kawatani, Y., Bushell, A. C., Holt, L., Serva, F., Anstey, J., Simpson, I. R., Osprey, S., Hamilton, K., Braesicke, P., Cagnazzo, C., Chen, C. C., Garcia, R. R., Gray, L. J., Kerzenmacher, T., Lott, F., McLandress, C., Naoe, H., Scinocca, J., Stockdale, T. N., Versick, S., Watanabe, S., Yoshida, K., and Yukimoto, S.: Response of the quasi-biennial oscillation to a warming climate in global climate models, Q. J. Roy. Meteorol. Soc., 148, 1490–1518, https://doi.org/10.1002/qj.3749, 2022.

Rodrigo, M., García-Serrano, J., and Bladé, I.: Quasi-biennial oscillation influence on tropical convection and El Niño variability, Geophys. Res. Lett., 52, https://doi.org/10.1029/2024GL112854, 2025.

Serva, F., Christiansen, B., Davini, P., von Hardenberg, J., van den Oord, G., Reerink, T. J., Wyser, K., and Yang, S.: Changes in stratospheric dynamics simulated by the EC-Earth model from CMIP5 to CMIP6, J. Adv. Model. Earth Syst., 16, e2023MS003756, https://doi.org/https://doi.org/10.1029/2023MS003756, 2024.

Smith, A. K., Holt, L. A., Garcia, R. R., Anstey, J. A., Serva, F., Butchart, N., Osprey, S., Bushell, A. C., Kawatani, Y., Kim, Y.-H., Lott, F., Braesicke, P., Cagnazzo, C., Chen, C. C., Chun, H.-Y., Gray, L., Kerzenmacher, T., Naoe, H., Richter, J., Versick, S., Schenzinger, V., Watanabe, S., and Yoshida, K.: The equatorial stratospheric semiannual oscillation and time-mean winds in QBOi models, Q. J. Roy. Meteorol. Soc., 148, 1593–1609, https://doi.org/10.1002/qj.3690, 2022.

Smith, A. K., Gray, L. J., and Garcia, R. R.: Evidence for the influence of the quasi-biennial oscillation on the semiannual oscillation in the tropical middle atmosphere, J. Atmos. Sci., 80, 1755–1769, https://doi.org/10.1175/JAS-D-22-0255.1, 2023.

https://doi.org/10.5194/egusphere-2026-2856
Preprint. Discussion started: 5 June 2026

Stockdale, T. N., Kim, Y.-H., Anstey, J. A., Palmeiro, F. M., Butchart, N., Scaife, A. A., Andrews, M., Bushell, A. C., Dobrynin, M., Garcia-Serrano, J., Hamilton, K., Kawatani, Y., Lott, F., McLandress, C., Naoe, H., Osprey, S., Pohlmann, H., Scinocca, J., Watanabe, S., Yoshida, K., and Yukimoto, S.: Prediction of the quasi-biennial oscillation with a multi-model ensemble of QBO-resolving models, Q. J. Roy. Meteorol. Soc., 148, 1519–1540, https://doi.org/10.1002/qj.3919, 2022.

Veenus, V. and Das, S. S.: The teleconnection between Brewer–Dobson circulation and quasi–biennial oscillation: Implications on ozone and water vapor distribution—a composite analysis, Clim. Dynam., 63, https://doi.org/10.1007/s00382-025-07616-9, 2025.

Wang, Y., Rao, J., Lu, Y., and Ju, Z.: QBO Disruption–like events in the China Meteorological Administration climate model, Adv. Atmos. Sci., 42, 1813–1832, https://doi.org/10.1007/s00376-025-4338-4, 2025.

Wheeler, M. and Kiladis, G. N.: Convectively coupled equatorial waves: Analysis of clouds and temperature in the wavenumber-frequency domain, J. Atmos. Sci., 56, https://doi.org/10.1175/1520-0469(1999)056<0374:CCEWAO>2.0.CO;2, 1999.

Yoo, C. and Son, S.-W.: Modulation of the boreal wintertime Madden-Julian oscillation by the stratospheric quasi-biennial oscillation, Geophys. Res. Lett., 43, 1392–1398, https://doi.org/10.1002/2016GL067762, 2016.